Generalized Multiphase-Shift Transient Modulation for Dual-Active-Bridge Series-Resonant Converter

Chuan Sun, *Student Member, IEEE*, Junwei Liu, *Member, IEEE*, Xingyue Jiang, Lingling Cao, *Member, IEEE*, Yun-Chong Wang, *Member, IEEE*, Jian-Xin Shen, *Senior Member, IEEE*, and Ka-Hong Loo, *Member, IEEE*

***Abstract*—Given the wide-range applications of bidirectional dual-active-bridge series-resonant converter (DABSRC), its complex nonlinear dynamic behavior is an interesting phenomenon that deserves attention of power electronics engineers. It is observed that if the control variables (i.e., phase-shift angles) are directly updated through conventional transient modulation, large-amplitude transient oscillations and dc offsets will be induced in the high-frequency-link voltages and currents during transient stage, which can ultimately degrade the converter's waveform quality significantly. The relatively few prior works in studying the transient oscillatory behavior of DABSRC have only focused on single-phase-shift modulation. In this article, a new transient modulation method referred to as generalized trajectory-switching modulation (GTSM) is first proposed for enhancing the transient performance of multiphase-shift modulated DABSRC. GTSM can simultaneously mitigate the problems of transient oscillations and dc offsets regardless of operation modes and power-flow directions, thus always ensuring safe transient operation. It also enables the resonant voltages and currents as well as magnetizing current to seamlessly reach the desired new steady-state values swiftly. Finally, the said theoretical claims are verified experimentally under both open loop and closed loop with model predictive control, and the influence of deviations from nominal resonant tank's parameters on GTSM is also considered.**

***Index Terms*—Dual-active-bridge (DAB), series-resonant converter (SRC), trajectory-switching modulation, transient performance.**

I. Introduction

FOR bidirectional isolated dc–dc power conversion, conventional inductor-based nonresonant dual-active-bridge converter (DABC) [1], [2] and *LC*-type DAB series-resonant converter (DABSRC) [3], [4] are both popular choices. As pointed out by some previous survey studies [5], [6], [7], [8], DABSRC can generally exhibit higher efficiency than DABC at the same power level. To further achieve higher efficiency over the whole power range, wider zero-voltage-switching (ZVS) range, minimum-tank-current operation, etc., numerous multiphase-shift (MPS), e.g., dual-phase-shift (DPS) and triple-phase-shift (TPS), modulation schemes were reported [9], [10], [11]. However, they target only steady-state optimization, and their impacts on DABSRC's dynamics remain unclear.

A major problem that exists in DABSRC is that, if the above-mentioned steady-state modulation schemes are utilized without transient trajectory planning, the pulsewidth-modulation (PWM) generator which attempts to introduce large-amplitude phase-shift increments/decrements directly in one step is susceptible to high-frequency transient oscillations, i.e., beat-frequency phenomenon [12], [13]. Such oscillations generally sustain for many switching cycles and result in high transient current and voltage stresses, additional power losses, and even permanent damage to power devices. Particularly when a fast and high-gain controller, such as the model-predictive controller (MPC) [14], [15], [16] is adopted, noticeable transient oscillations will appear, thus resulting in significant adverse impacts on the transient performance. To avoid the problems of transient oscillations, until now only a limited number of researches have been done to explore different approaches in control and modulation. In [12], a dual-loop controller is designed based on the small-signal model of DABSRC. However, this study only suggests to select low-gain control parameters, which inevitably leads to slow transient responses. In general, a controller's bandwidth is much lower than the beat frequency of DABSRC, and hence the method based on classical control theory cannot provide satisfactory solutions against high-frequency oscillations. To achieve optimal dynamics, further improvements in transient modulation strategies are necessary in addition to using well-designed controllers.

How to effectively alter the trajectories of resonant currents and voltages represents a challenging research problem. Recently, four optimized transient single-phase-shift (SPS) modulation strategies were proposed for DABSRC in [17], [18], and [19]. Unfortunately, they are designed with complicated trajectory-constrained conditions, and closed-form expressions of their modulation laws are not available. Thus, they generally

Manuscript received 19 November 2022; revised 5 March 2023; accepted 10 April 2023. Date of publication 14 April 2023; date of current version 19 May 2023. This work was supported in part by the Innovation, Technology Fund Midstream Research Programme for Universities under Grant MRP/019/21X, and in part by the Research Institute for Smart Energy (RISE) under Grant P0039680. Recommended for publication by Associate Editor D. Maksimovic. *(Corresponding author: Ka-Hong Loo.)*

Chuan Sun, Junwei Liu, Xingyue Jiang, and Ka-Hong Loo are with the Department of Electronic and Information Engineering, The Hong Kong Polytechnic University, Hong Kong (e-mail: chuan.sun@connect.polyu.hk; liujunwei_hust@hotmail.com; xingyue.jiang@connect.polyu.hk; kh.loo@polyu.edu.hk).

Lingling Cao is with the School of Mechanical Engineering and Automation, Harbin Institute of Technology, Shenzhen 518055, China (e-mail: caolingling@hit.edu.cn).

Yun-Chong Wang and Jian-Xin Shen are with the College of Electrical Engineering, Zhejiang University, Hangzhou 310027, China (e-mail: wangycee@zju.edu.cn; j_x_shen@zju.edu.cn).

Color versions of one or more figures in this article are available at https://doi.org/10.1109/TPEL.2023.3267297.

Digital Object Identifier 10.1109/TPEL.2023.3267297

0885-8993 © 2023 IEEE. Personal use is permitted, but republication/redistribution requires IEEE permission.
See https://www.ieee.org/publications/rights/index.html for more information.

Authorized licensed use limited to: Macau Univ of Science and Technology. Downloaded on May 08,2025 at 08:12:51 UTC from IEEE Xplore. Restrictions apply.

require excessive sensing in the converter, and their transient pulsewidths must be predefined and precalculated. Obviously, due to their high computational and implementation complexity, it is unfeasible to extend such methods to MPS-modulated DABSRC. In addition, it can be observed from the experimental results that all these modulation schemes are only executed once under open-loop conditions. However, it is well understood that it is difficult or even impossible to reach a new steady state within only one switching cycle in a real-time closed-loop controlled DABSRC, particularly under large-amplitude disturbances. As external load disturbances are often uncertain, the practical usefulness of these methods when implemented in closed-loop systems is limited. In [13], another scheme known as trajectory-switching modulation (TSM) can provide accurate closed-form expressions of its transient pulsewidths, and it is capable of sensorless operation, which is a simpler and more desirable solution. However, the feasible solution region of TSM becomes restricted when the applied switching frequency (f_s) approaches the resonant frequency (f_r). In order to achieve a wider operating range under TSM, v_{cd} is modified when increasing the phase-shift angle, while v_{ab} is modified when decreasing the phase-shift angle, which makes it inconvenient to use in MPS-modulated DABSRC.

As all the transient modulation schemes employed in [13], [17], [18], and [19] can effectively suppress transient oscillations, it is anticipated that their performance differences under open-loop conditions are relatively small. Hence, the algorithm's complexity should be a major consideration. In addition, there are two obvious methodological limitations with the existing approaches. The first limitation is that they are designed to be compatible with SPS modulation only. Since SPS modulation has limitations in ZVS range, peak current stress, backflow power, etc., at different converter gains and power levels, it is worthwhile to develop a new transient modulation strategy for MPS gating schemes. The second limitation is that all of them are unable to eliminate the transient dc offset in transformer's magnetizing current, which will result in a potential risk of transformer's core saturation and longer settling time during transient state, thus inevitably degrading the transient performance of DABSRC. Therefore, how to further improve the dynamics of closed-loop controlled and MPS-modulated DABSRC is of great interest and has become an actively researched topic in both academic and industry.

In light of the above, this article proposes a new transient modulation strategy known as generalized TSM (GTSM) for realizing optimal dynamic performance in MPS-modulated DABSRC. The main contributions of the proposed GTSM and this study can be summarized as follows:

1) GTSM can be applied universally to any MPS gating schemes, operation modes, and power-flow directions, making it compatible with essentially most applications.
2) GTSM represents the first method that can suppress the transient oscillations and dc offsets simultaneously.
3) Unlike the existing technique (TSM [13]), GTSM can be utilized effectively even when the switching-to-resonant frequency ratio $F = f_s/f_r$ is small. Hence, the designed transient pulsewidths of GTSM are easily modified with respect to a fixed reference signal.
4) The algorithm of GTSM is guided by a set of analytical expressions and does not require any voltage or current feedback (i.e., sensorless), which facilitates its cycle-by-cycle implementation in an accurate and cost-effectively manner under closed-loop conditions.
5) A combined use of GTSM and MPC is presented for demonstrating the merits of GTSM under closed-loop conditions when coupled with a fast controller.
6) An online parameter estimation method is employed to ensure both GTSM and MPC can adaptively work well when the resonant tank's parameters are not precisely known or deviate significantly from the nominal values.

TABLE I
COMPARISON OF DIFFERENT TRANSIENT MODULATION SCHEMES

Desirable properties	GTSM	TSM [13]	Methods in [17]–[19]
Oscillation suppression	✓	✓	✓
DC-offset elimination	✓	✗	✗
Generic method	✓	✗	✗
Analytical expression	✓	✓	✗
Sensorless algorithm	✓	✓	✗
Closed-loop implementation	✓	✓	✗
Wide feasible region	✓	✗	Not applicable

Table I compares different transient modulation techniques for DABSRC. As GTSM can achieve all desirable properties, it is an ideal and by far the most effective scheme.

The rest of this article is organized as follows. Section II describes an independent half-bridge equivalent circuit model of TPS-modulated DABSRC and the conventional transient modulation scheme. The fundamental principle of the proposed GTSM strategy is presented in Section III. In Section IV, a closed-loop MPC design for MPS-modulated DABSRC is presented, followed by the online estimation of resonant tank's parameters in Section V. Experimental results and data analysis are shown in Section VI. Finally, Section VII concludes this article.

II. INDEPENDENT HALF-BRIDGE EQUIVALENT MODEL AND CONVENTIONAL TRANSIENT MODULATION

Fig. 1 illustrates the circuit schematic of DABSRC. The L_r-C_r series-resonant tank, in fact, acts as a filter to attenuate the high-frequency harmonics of ac-link currents and voltages to produce near sinusoidal current i_r from square-wave (or quasi-square-wave) voltages v_{ab} and v_{cd}. L_s and L_m are the secondary-side leakage inductance and equivalent magnetizing inductance, respectively, and the transformer's turns ratio is $N:1$. It is defined as forward-power mode when energy flows from V_1 (dc input voltage) to V_2 (dc output voltage). The load resistance is represented by R_L, and the load current is I_o. The total output capacitance is C_o, and its value can be greatly reduced by designing a fast-response control loop.

Authorized licensed use limited to: Macau Univ of Science and Technology. Downloaded on May 08,2025 at 08:12:51 UTC from IEEE Xplore. Restrictions apply.

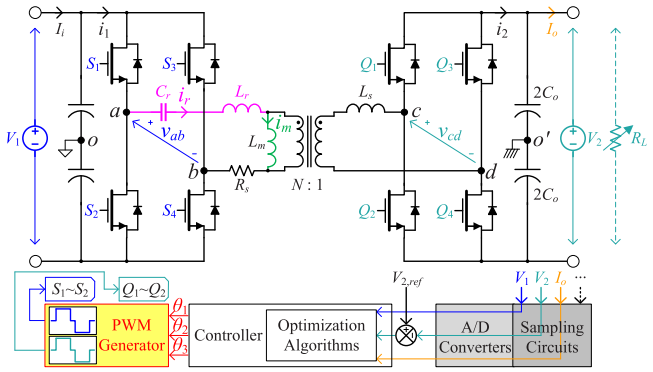

Fig. 1. Circuit schematic of DABSRC.

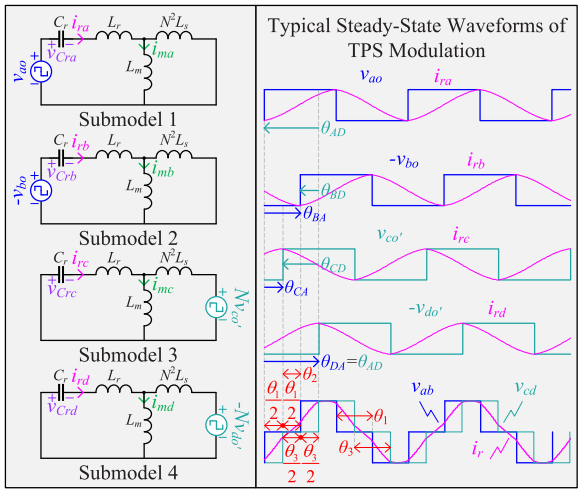

Fig. 2. Independent half-bridge equivalent model and steady-state waveforms of TPS-modulated DABSRC.

As shown in Fig. 2, referring to the analyses presented in [20], v_{ab} and v_{cd} under any MPS modulation schemes can be seen as produced by four half-bridge square-wave generators (i.e., v_{ao}, $-v_{bo}$, $v_{co'}$, and $-v_{do'}$), which are phase-shifted from each other by $\{\theta_{BA}, \theta_{CA}, \theta_{DA}\}$ (i.e., with respect to v_{ao}) or $\{\theta_{AD}, \theta_{BD}, \theta_{CD}\}$ (i.e., with respect to $-v_{do'}$) for achieving different power levels and flow directions. Thus, a DABSRC can be further decomposed into four independent half-bridge equivalent circuit submodels, which helps us in analyzing the resonant current i_r, magnetizing current i_m, and resonant capacitor voltage v_{Cr} by calculating the contribution of each independent excitation source separately. Using the superposition theorem yields

$$\begin{cases} i_r = i_{ra} + i_{rb} + i_{rc} + i_{rd} \\ i_m = i_{ma} + i_{mb} + i_{mc} + i_{md} \\ v_{Cr} = v_{\mathrm{Cra}} + v_{\mathrm{Crb}} + v_{\mathrm{Crc}} + v_{\mathrm{Crd}}. \end{cases} \tag{1}$$

Accordingly, by applying mesh analysis to for example submodel 2 and submodel 3, we obtain

$$i_{mb} = \frac{N^2 L_s}{L_m + N^2 L_s} i_{rb} \tag{2}$$

TABLE II
RELATIONS BETWEEN DIFFERENT DEFINITIONS OF PHASE-SHIFT ANGLES

Reference Signal	Phase-Shift Relationship
v_{ao}	$\theta_{BA} = \theta_1$
	$\theta_{CA} = \theta_2 + 0.5 * (\theta_1 - \theta_3)$
	$\theta_{DA} = \theta_2 + 0.5 * (\theta_1 + \theta_3)$
$-v_{do'}$	$\theta_{AD} = \theta_2 + 0.5 * (\theta_1 + \theta_3)$
	$\theta_{BD} = \theta_2 + 0.5 * (\theta_3 - \theta_1)$
	$\theta_{CD} = \theta_3$

$$i_{mc} = \left(\frac{1}{\omega_s^2 L_m C_r} - \frac{L_r}{L_m} \right) i_{rc} \tag{3}$$

where $\omega_s = 2\pi f_s$.

Typically, under TPS modulation, the following definitions of phase-shift angles are adopted: $\theta_1 \in [0, \pi]$ and $\theta_3 \in [0, \pi]$ as the inner phase-shift angles of the primary and secondary bridges, and $\theta_2 \in [-\pi/2, \pi/2]$ as the outer phase-shift angle. In our case, based on the selected reference signal, i.e., either v_{ao} or $-v_{do'}$, the relations between different phase-shift angles are tabulated in Table II. In general, for conventional transient phase-shift modulation (CTPSM), v_{ao} is set as a frequency-fixed 50% duty-cycle square-wave reference signal. During transient state, the low-level durations of $-v_{bo}$, $v_{co'}$ and $-v_{do'}$ are directly increased/decreased by $\Delta\theta_{BA}$, $\Delta\theta_{CA}$, and $\Delta\theta_{DA}$, respectively, with respect to v_{ao}. However, it is known that the direct adjustments of θ_{BA}, θ_{CA}, and θ_{DA} (or the three control variables θ_1, θ_2, and θ_3) will induce complex dynamics in i_r, i_m, v_{Cr}, etc.

Fig. 3 presents an open-loop simulation example of how these phase-shift angles are updated by CTPSM. It is assumed that the desired phase-shift increments/decrements are $\Delta\theta_1$, $\Delta\theta_2$, and $\Delta\theta_3$. In this simulation test, the scenario $\theta_1 = 0, \theta_2 = \pi/9$, $\theta_3 = 0$, $\Delta\theta_1 = \pi/6$, $\Delta\theta_2 = 11\pi/36$, and $\Delta\theta_3 = \pi/9$, i.e., a transition from SPS mode to TPS mode is simulated. In addition, $V_1 = 110$ V, $V_2 = 100$ V, $f_s = 60$ kHz, $f_r = 38.96$ kHz, $F = f_s/f_r = 1.54$, and other simulation parameters can be found in Table III. It can be seen from Fig. 3(a) that high-frequency transient oscillations are induced in i_{rb}, i_{rc}, i_{rd}, i_r, v_{Crb}, v_{Crc}, v_{Crd}, and v_{Cr}, and excessive transient dc offsets appear in i_{mb}, i_{mc}, i_{md}, and i_m. However, such situations do not arise in the branch currents and voltages of submodel 1. This suggests that only when a direct pulsewidth adjustment occurs in any of these independent square-wave voltages will transient oscillations and dc offsets be generated in DABSRC. Based on the state-plane trajectories shown in Fig. 3(b), the transient voltage and current stresses can reach nearly twice the new steady-state values under open-loop simulations, which increases the device stress, risk of system failure, and electromagnetic interference (EMI) noise. In addition, this particular oscillation phenomenon can last for dozens of switching cycles, although it will gradually decay as the transient energy can be dissipated in the parasitic resistance of the circuit. As all the problems are attributed to the use of CTPSM, more advanced transient phase-shift modulation scheme should be studied.

Authorized licensed use limited to: Macau Univ of Science and Technology. Downloaded on May 08,2025 at 08:12:51 UTC from IEEE Xplore. Restrictions apply.

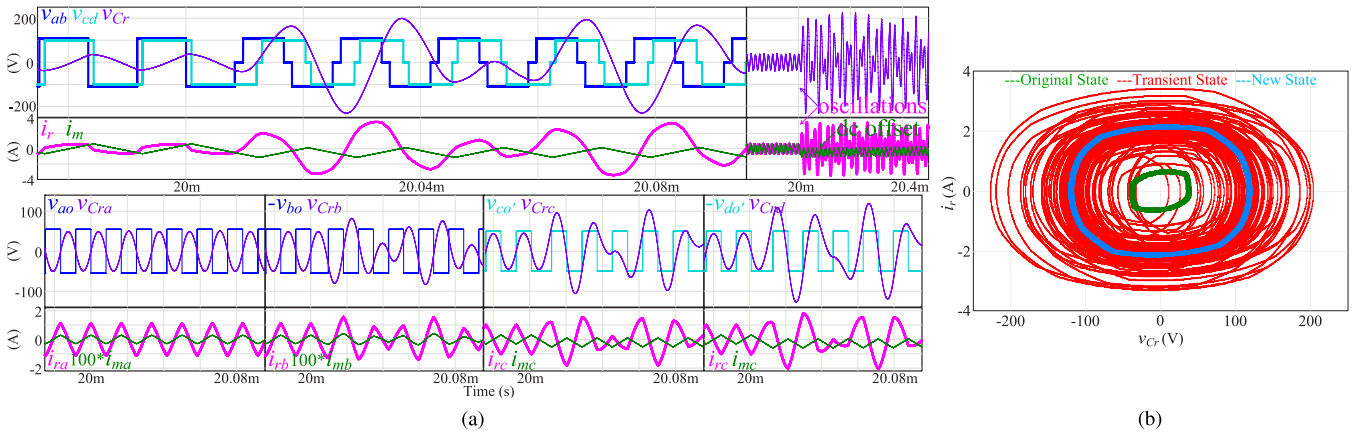

Fig. 3. Open-loop simulation example from SPS mode to TPS mode under CTPSM with $V_1 = 110$ V, $V_2 = 100$ V, $f_s = 60$ kHz, and $F = 1.54$. (a) Simulated transient waveforms. (b) v_{Cr}-i_r state-plane diagram under CTPSM.

TABLE III
CIRCUIT PARAMETERS USED IN EXPERIMENTS AND SIMULATIONS

Symbol	Parameter Description	Value or Part Type
V_1	Input Voltage	110-125 V
V_2	Output Voltage	100 V
C_o	Output Capacitance	47 μF
R_L	Load Resistance	50/200 Ω
$N:1$	Transformer's Turns Ratio	1 : 1
L_m	Magnetizing Inductance	650 μH
L_r	Resonant Inductance	321 μH
L_s	Secondary Inductance	1.70 μH
C_r	Resonant Capacitance	52 nF
f_s	Switching Frequency	50-60 kHz
f_r	Resonant Frequency	38.96 kHz
S_x~Q_x	Power Switches	UnitedSiC UJC06505K
–	Dead Time	250 ns
–	Gate Driver	TI UCC21520
–	Current Transducer	LEM LA 55-P
–	Voltage Transducer	Resistive Divider
–	Microprocessor	TI TMS320F28335
–	DAC Module	Microchip MCP4921
–	Simulation Platform	Powersim PSIM

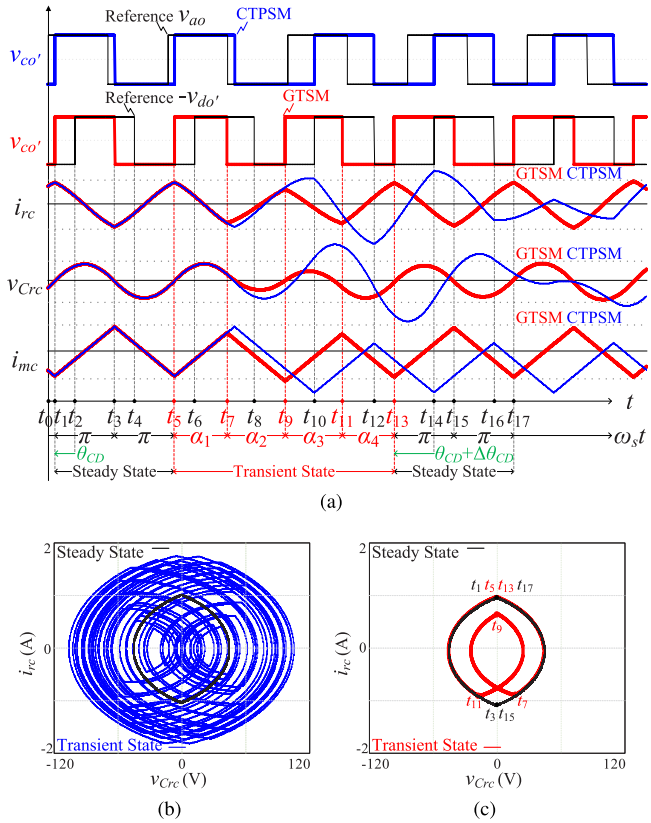

Fig. 4. (a) Theoretical transient waveforms with CTPSM and the proposed GTSM in submodel 3. (b) $v_{\rm Crc}$-i_{rc} state-plane diagram under CTPSM. (c) $v_{\rm Crc}$-i_{rc} state-plane diagram under GTSM.

III. PROPOSED GTSM STRATEGY

A fundamental property illustrated by the analysis presented in Section II is that, although the currents and voltages in different submodels exhibit different degrees of transient behaviors, if oscillation-free and dc-offset-free transient responses are achieved in each of these four submodels by separately applying an appropriate transient square-wave excitation to the submodel, smooth transitions can be achieved in i_r, i_m, and v_{Cr} simultaneously by the principle of superposition. As an illustration example, we will analyze the transient response of one submodel, such as submodel 3 with excitation source $v_{co'}$. As labeled in Fig. 4(a), for the proposed GTSM, there are four transient modulation variables, namely, α_1, α_2, α_3, and α_4. Instead of using CTPSM to directly update the phase-shift increment in one step, the proposed GTSM attempts to execute the phase-shift adjustment in multiple steps, which means that more degrees of freedom (DOF) are available for trajectory planning and control by GTSM during transient state. The key point of the proposed GTSM is that the ac-link current and voltage trajectories of DABSRC should be modified by α_1,

Authorized licensed use limited to: Macau Univ of Science and Technology. Downloaded on May 08,2025 at 08:12:51 UTC from IEEE Xplore. Restrictions apply.

α_2, α_3, and α_4 to fulfil the boundary conditions for realizing oscillation-free transition [13] and dynamic volt-second balance for eliminating transient dc offset [20], [21].

A. Elimination of Transient DC Offset

Typically, if v_{ao} is selected as the reference signal under CTPSM, the direct changes in $-v_{bo}$, $v_{co'}$, and $-v_{do'}$ during transient state will inevitably lead to excessive transient dc offsets in i_{mb}, i_{mc}, and i_{md}. However, according to (2), the transient dc offsets in i_{ma} and i_{mb} are relatively small, and i_{mc} and i_{md} will have stronger influences on i_m due to $L_m > L_r \gg L_s$ in most applications of DABSRC. As any transient operation in the secondary-side voltages may result in large-amplitude transient current in i_{mc} and/or i_{md} and long settling time, it is suggested that $-v_{do'}$ is fixed and used as the reference signal and phase-shift adjustments are accomplished through the modifications of v_{ao}, $-v_{bo}$, and $v_{co'}$. For this reason, $-v_{do'}$ is set as a fixed reference signal under GTSM, and θ_{AD}, θ_{BD}, and θ_{CD} are expressed in terms of θ_1, θ_2, and θ_3, as given in Table II.

However, the setting of appropriate reference signal alone cannot eliminate the transient dc offset in i_m. In fact, (2) and (3) also show that the current flowing through the magnetizing inductance branch (e.g., i_{mb} or i_{mc}) is directly proportional to the current flowing through the L_r-C_r resonant network branch (e.g., i_{rb} or i_{rc}). Hence, supposing that the submodel circuits are purely inductive, to eliminate transient dc offset in i_{mc}, a dynamic volt–second balance should be imposed on $v_{co'}$ [20]. Consequently, in submodel 3, a constraint condition of the volt-second balance during transient state is given by

$$\begin{aligned} Nv_{co'}\alpha_1 - Nv_{co'}\alpha_2 + Nv_{co'}\alpha_3 - Nv_{co'}\alpha_4 = 0 \\ \Rightarrow \alpha_1 - \alpha_2 + \alpha_3 - \alpha_4 = 0. \end{aligned} \tag{4}$$

In addition, to ensure that the transient state ends no later than t_{13} under GTSM, it can be found from Fig. 4(a) that a phase-shift constraint is required as

$$\omega_s(t_{13} - t_5) = \alpha_1 + \alpha_2 + \alpha_3 + \alpha_4 = 4\pi - \Delta\theta_{CD}. \tag{5}$$

Combining (4) and (5) leads to

$$\alpha_1 + \alpha_3 = \alpha_2 + \alpha_4 = 2\pi - 0.5\Delta\theta_{CD} \tag{6}$$

and the use of (6) will ensure that i_{mc} enters its new steady state before t_{13}.

As discussed in [21], in order to minimize the adverse effects caused by transient dc offset, it is important to minimize the time-averaged value of i_{mc} (i.e., $\bar{i_{mc}}$) over the transient state. By applying constraint (6), $\bar{i_{mc}}$ can be simplified and expressed as

$$\begin{aligned} \bar{i_{mc}} &= \frac{1}{t_{13}-t_5}\int_{t_5}^{t_{13}} i_{mc}\mathrm{d}t \\ &= \frac{NV_2}{2L_m}\left(-\frac{T_s}{4} + \frac{2\pi - 0.5\Delta\theta_{CD}}{2} - \frac{\alpha_2\alpha_3}{2\pi - 0.5\Delta\theta_{CD}}\right) \end{aligned} \tag{7}$$

where $T_s = 1/f_s$ is the switching period. It can be deduced from (7) that for a given $\Delta\theta_{CD}$, $\bar{i_{mc}}$ reaches its minimum value only when $\alpha_2 = \alpha_3$ and both α_2 and α_3 are set to their maximum possible values, namely,

$$\alpha_2 = \alpha_3 = \max(\alpha_2) = \max(\alpha_3). \tag{8}$$

Thus, (8) is the optimal solution of (6) for eliminating transient dc offset and achieving a minimum $\bar{i_{mc}}$ during transient state.

B. Elimination of High-Frequency Transient Oscillations

It should be noted that with (6) and/or (8), the values of α_1, α_2, α_3, and α_4 cannot be uniquely determined. In other words, (6) merely guarantees the elimination of transient dc offset but cannot guarantee the elimination of transient oscillations in i_{rc} and v_{Cr}.

Referring to our previous research work reported in [13], the analytical expressions of i_r and v_{Cr} for an ideal L_r-C_r tank can be obtained by applying the Kirchhoff's voltage law to the equivalent circuit of DABSRC. Similarly, by neglecting the magnetizing inductance L_m of submodel 3, i.e., L_m is treated as open circuit, i_{rc} and v_{Crc} are expressed by (9) and (10), respectively,

$$\begin{aligned} i_{rc}(t) &= i_{rc}(t_i)\cos(\omega_r(t-t_i)) \\ &\quad + ((-Nv_{co'}) - v_{\mathrm{Crc}}(t_i))\sin(\omega_r(t-t_i))/Z_r \end{aligned} \tag{9}$$

$$\begin{aligned} v_{\mathrm{Crc}}(t) &= v_{\mathrm{Crc}}(t_i)\cos(\omega_r(t-t_i)) + Z_r i_{rc}(t_i)\sin(\omega_r(t-t_i)) \\ &\quad + (-Nv_{co'})(1-\cos(\omega_r(t-t_i))) \end{aligned} \tag{10}$$

where $Z_r = \sqrt{L_r/C_r}$ represents the characteristic impedance of the resonant tank, $\omega_r = 1/\sqrt{L_rC_r} = 2\pi f_r$ is the angular resonant frequency, and the subscript $i = 1, 2, 3, \ldots$ is used to indicate the time nodes.

Due to the symmetrical characteristics of the steady-state waveforms shown in Fig. 4, the initial steady-state values of i_{rc} and v_{Crc} at the beginning of the transient state (t_5) are given by

$$i_{rc}(t_5) = i_{rc}(t_1) = -i_{rc}(t_3) = NV_2\tan(\pi/2/F)/2/Z_r \tag{11}$$

$$v_{\mathrm{Crc}}(t_5) = v_{\mathrm{Crc}}(t_1) = -v_{\mathrm{Crc}}(t_3) = 0 \tag{12}$$

and the values of $i_{rc}(t_5)$ and $v_{\mathrm{Crc}}(t_5)$ are constant for a given set of circuit parameters and operating conditions. All of the following instantaneous values of i_{rc} and v_{Crc} at other time instances can be found by iteratively applying (9) and (10). For example, the upper boundary values of i_{rc} and v_{Crc} at the end of the transient state (t_{13}) are given by

$$\begin{aligned} i_{rc}(t_{13}) &= \frac{NV_2}{2Z_r}\sec\left[\frac{\pi}{2F}\right]\left(\sin\left[\frac{\pi - 2(\alpha_1+\alpha_2+\alpha_3+\alpha_4)}{2F}\right]\right. \\ &\quad + 2\cos\left[\frac{\pi}{2F}\right]\left(\sin\left[\frac{\alpha_4}{F}\right] - \sin\left[\frac{\alpha_3+\alpha_4}{F}\right]\right. \\ &\quad \left.\left. + \sin\left[\frac{\alpha_2+\alpha_3+\alpha_4}{F}\right]\right)\right) \end{aligned} \tag{13}$$

Authorized licensed use limited to: Macau Univ of Science and Technology. Downloaded on May 08,2025 at 08:12:51 UTC from IEEE Xplore. Restrictions apply.

$$v_{\text{Crc}}(t_{13}) = \frac{NV_2}{2}\sec\left[\frac{\pi}{2F}\right]\left(\cos\left[\frac{\pi-2(\alpha_1+\alpha_2+\alpha_3+\alpha_4)}{2F}\right]+\cos\left[\frac{\pi}{2F}\right]\left(1-2\left(\cos\left[\frac{\alpha_4}{F}\right]-\cos\left[\frac{\alpha_3+\alpha_4}{F}\right]+\cos\left[\frac{\alpha_2+\alpha_3+\alpha_4}{F}\right]\right)\right)\right). \tag{14}$$

As the objective of GTSM is to suitably design the transient pulsewidths (i.e., α_1 to α_4) to fulfil the required phase-shift adjustments (5) commanded by the controller while ensuring that the transient values of v_{Crc} and i_{rc} can reach the targeted new steady-state values at the designated time (e.g., t_{13}) and will remain in the same convergent state after that. The sufficient and necessary condition for effectively suppressing the transient oscillations in i_{rc} and v_{Crc} is that their new steady-state values at t_{13} should be equal to their initial steady-state values at t_5. Hence,

$$\begin{cases} i_{rc}(t_{13}) = i_{rc}(t_5) \\ v_{\text{Crc}}(t_{13}) = v_{\text{Crc}}(t_5). \end{cases} \tag{15}$$

It should be noted that since $C_r\Delta v_{\text{Crc}} = \int i_{rc}\mathrm{d}t$, $v_{\text{Crc}}(t_{13}) = v_{\text{Crc}}(t_5)$ in fact guarantees a dynamic amp-second balance in the resonant capacitor. Substituting (11), (12), (13), and (14) into (15) leads to

$$\cos\left[\frac{\pi}{2F}\right]\left(\sin\left[\frac{\alpha_4}{F}\right]-\sin\left[\frac{\alpha_3+\alpha_4}{F}\right]+\sin\left[\frac{\alpha_2+\alpha_3+\alpha_4}{F}\right]\right) = \sin\left[\frac{\alpha_1+\alpha_2+\alpha_3+\alpha_4}{2F}\right]\cos\left[\frac{\alpha_1+\alpha_2+\alpha_3+\alpha_4-\pi}{2F}\right] \tag{16}$$

$$\cos\left[\frac{\pi}{2F}\right]\left(\cos\left[\frac{\alpha_4}{F}\right]-\cos\left[\frac{\alpha_3+\alpha_4}{F}\right]+\cos\left[\frac{\alpha_2+\alpha_3+\alpha_4}{F}\right]\right) = \cos\left[\frac{\alpha_1+\alpha_2+\alpha_3+\alpha_4}{2F}\right]\cos\left[\frac{\alpha_1+\alpha_2+\alpha_3+\alpha_4-\pi}{2F}\right] \tag{17}$$

which are used as the current and voltage constraints, respectively, for GTSM. A combination of (5), (16), and (17) in fact forms a 4-DOF general solution for the suppression of transient oscillations in i_{rc} and v_{Crc}, and solving these three simultaneous equations yields a simplified constraint condition given by

$$2\cos\left[\frac{\alpha_3+\alpha_4-\alpha_1}{2F}\right]\sin\left[\frac{\alpha_2}{2F}\right] = \sin\left[\frac{2\pi-0.5\Delta\theta_{CD}-\alpha_4}{F}\right]. \tag{18}$$

C. GTSM—An Optimal 4-DOF Transient Phase-Shift Modulation for Oscillation-Free and DC-Offset-Free Dynamics

Based on the analysis presented in Sections III-A and III-B, the realization of oscillation-free and dc-offset-free dynamics in submodel 3 should simultaneously satisfy at least two constraints, i.e., (6) and (18), in order to achieve the stated objectives before t_{13}. Substituting (6) into (18) gives

$$\cos\left[\frac{\alpha_3+\alpha_4-\alpha_1}{2F}\right] = \cos\left[\frac{\alpha_2}{2F}\right] \tag{19}$$

and hence $\alpha_3+\alpha_4-\alpha_1 = \pm\alpha_2$. Through a careful analysis, only one particular solution set, i.e., the proposed GTSM (20), is found to be practically feasible given that the transient pulsewidths must be greater than zero

$$\begin{cases} \alpha_1 = \alpha_4 = 2\pi - 0.5\Delta\theta_{CD} - \alpha_2 \\ \alpha_2 = \alpha_3 = F\arccos\left[\frac{1+\cos\left[\frac{3\pi-\Delta\theta_{CD}}{2F}\right]\sec\left[\frac{\pi}{2F}\right]}{2}\right]. \end{cases} \tag{20}$$

Fig. 4(b) and (c) illustrate the simulated v_{Crc}-i_{rc} state-plane diagrams under CTPSM and GTSM, respectively. Compared with CTPSM, the transient trajectories under GTSM can converge rapidly (one to two switching cycles) to the steady-state elliptic trajectory (i.e., the black curve) without any overshoots and oscillations. Besides, (20) also specifies the boundary values of α_2 and α_3 needed to minimize the transient dc offset in accordance with (8). As evident from (20), no sensor is required by the proposed GTSM, and it only relies on F (a nearly constant parameter) and the phase-shift increment or decrement ($\Delta\theta_{CD}$) obtained from the controller. The symmetrical PWM pattern of GTSM also facilitates its cycle-by-cycle implementation in the PWM modules inside the microcontroller.

Similarly, by substituting $\Delta\theta_{CD}$ with $\Delta\theta_{AD}$ and $\Delta\theta_{BD}$ into (20), the GTSM schemes for submodels 1 and 2 (i.e., v_{ao}, $-v_{bo}$) can be obtained similarly, while submodel 4 is excited by a square-wave voltage $-v_{do'}$ of 50% duty cycle. By separately applying GTSM to the four submodels which guarantees their smooth transitions from the old to the new steady states, an overall oscillation-free and dc-offset-free transient response can be ensured for MPS-modulated DABSRC.

D. Performance Evaluation of Different Transient Modulation Strategies for DABSRC

The transient modulation strategies reported in the prior works [17], [18], [19] require the adjustments of the high- and/or low-level durations of both v_{ab} and v_{cd} during each execution, which leads to high implementation complexity and complicated relationships between modulation variables. The transient pulsewidths under these methods cannot be decoupled from the state variables and feedback information of DABSRC, and there are generally no analytical solution available for implementation, hence numerical solutions are used instead. However, in closed-loop implementation of DABSRC, it is impossible to obtain the precise transient pulsewidths in each switching cycle due to discretization error, which causes the performances and effectiveness of these methods to degrade in practice.

It can be further verified that the 3-DOF TSM strategy proposed in [13] is a particular solution of the generalized 4-DOF strategy given by (18) of this article, and there exists no feasible 2-DOF modulation schemes for (18), where two of the four modulation variables are π. By letting $\{\alpha_1 > 0, \alpha_2 > 0, \alpha_3 > 0, \alpha_4 > 0\}$, the feasible regions of both TSM and GTSM are compared in Fig. 5. In case of a sufficiently large F, there are solutions for both $\Delta\theta_2 > 0$ and $\Delta\theta_2 < 0$, and hence TSM can be applied in any submodels without changing the reference signal. However, when F is small, the feasible region of TSM becomes narrow and there is no solution for $\Delta\theta_2 < 0$, in which case the

Authorized licensed use limited to: Macau Univ of Science and Technology. Downloaded on May 08,2025 at 08:12:51 UTC from IEEE Xplore. Restrictions apply.

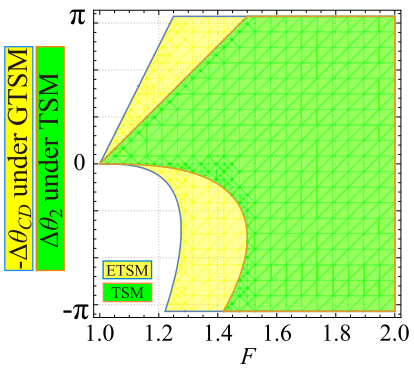

Fig. 5. Feasible regions of GTSM and TSM.

reference signal of TSM should be changed to avoid a negative phase-shift change. This is the reason of why TSM is implemented in v_{cd} for $\Delta\theta_2 > 0$ and v_{ab} for $\Delta\theta_2 < 0$ in [13], which makes it extremely difficult to apply TSM to MPS-modulated DABSRC when F is small. It can be seen from Fig. 5 that the proposed GTSM can be utilized over a wide range of f_s (i.e., it produces feasible solutions for small F), and its feasible region is much larger than that of TSM. Hence, GTSM can be applied in any of the submodels without altering the relation between the reference excitation source and the other excitation sources. This makes GTSM easy to use in MPS-modulated DABSRC, which is an important advantage of GTSM over all existing transient modulation methods presented in [13], [17], [18], and [19].

Fig. 6(a) and (c) show the simulated transient waveforms of DABSRC under TSM and GTSM with large F ($F = 1.54$). Other circuit parameters are the same as those used in Fig. 3. It can be seen that although TSM is able to suppress transient oscillations, it still leads to excessive transient dc offsets in i_m and some overshoots in v_{Cr}, while GTSM can achieve a transient performance without overshoot, transient dc offset, and transient oscillations. From the state-plane diagrams shown in Fig. 6(b) and (d), GTSM constantly produces lower energy trajectories of i_r and v_{Cr}, as the transient trajectories under GTSM are closer to the desired new-steady-state trajectories. Therefore, GTSM represents a significant improvement over TSM, even when F is large.

Going one step further, when $F \to \infty$, traditional DABC can be regarded as a special case of DABSRC with infinite C_r [7]. Accordingly, by taking the limits, (20) can be simplified to (21) for eliminating the transient dc offsets in both inductor and transformer's magnetizing currents of a conventional DABC, which demonstrates the generality of the proposed solution (20)

$$\begin{cases} \alpha_1 = \alpha_4 = \pi - 0.5\Delta\theta_{CD} \\ \alpha_2 = \alpha_3 = \lim\limits_{F\to\infty} F \arccos\left[\dfrac{1+\cos\left[\frac{3\pi-\Delta\theta_{CD}}{2F}\right]\sec\left[\frac{\pi}{2F}\right]}{2}\right] = \pi. \end{cases} \tag{21}$$

It should be noted that, unlike the piecewise-linear inductor current in DABC that can directly reach a specific value by linearly adjusting the turn-on and turn-off pulsewidths of some power switches, the trajectory of the nonlinear resonant current in DABSRC cannot be easily modified to follow the changes in pulse durations instantaneously. Accordingly, the constraints for transient dc-offset elimination in DABC are linear equations, whereas the constraints for transient oscillation suppression in DABSRC are nonlinear transcendental equations. Although some optimized transient phase-shift modulation strategies have been developed to eliminate transient dc offsets in DABC [20], [21], [22], [23], they cannot be applied to mitigate transient oscillations in DABSRC. Besides, the prior transient modulation schemes proposed for DABSRC in [13], [17], [18], [19] were designed to eliminate transient oscillations only, hence they have failed to eliminate the transient dc offset, which is more important for DABC. For example, the three transient modulation variables of TSM reported in [13] can be simplified to $\{\pi + 0.25\Delta\theta_2, \pi + 0.5\Delta\theta_2, \pi + 0.25\Delta\theta_2\}$ as F approaches infinity. In this case, TSM can eliminate transient dc offset in i_r but fails to eliminate transient dc offset in i_m. In fact, compared with the simulation result shown in Fig. 3(a) under CTPSM, TSM causes a more severe transient dc offset in i_m, as can be seen from Fig. 6(c).

In summary: 1) GTSM has a wide operating range and can simultaneously achieve oscillation-free and dc-offset-free convergence to the new steady state within one to two switching cycles in MPS-modulated DABSRC. It is viewed as the most effective transient modulation scheme for DABSRC up to date. 2) Until now, the proposed GTSM strategy is the only unified approach capable of simultaneously eliminating transient oscillations and dc offsets in both MPS-modulated DABC and DABSRC. 3) A transient modulation scheme developed for DABSRC may be applicable to DABC (e.g., GTSM), but the inverse is not true. 4) Except for the proposed GTSM, all existing transient modulation schemes developed for DABSRC cannot be used to eliminate transient dc offsets in i_r and i_m of DABC.

IV. Model Predictive Control With Minimum-RMS-Current Operation

Although the above open-loop simulation results enable us to compare the transient performances of CTPSM and GTSM in response to single-step changes in phase-shift angles, DABSRC is generally operated in closed-loop configuration in practice. Thus, to demonstrate its practical values, the proposed GTSM should be implementable on a cycle-by-cycle basis under closed-loop conditions. It should be noted that the proposed GTSM can be implemented with any controller, but as explained in [13] and [21], fast controllers are preferred since their inherently wide control bandwidth will induce abrupt and large-amplitude changes in phase-shift angles. Therefore, in this article, the transient performance of GTSM under closed-loop conditions is verified using a high-gain MPC with minimum root-mean-square (rms) current operation similar to the one developed for MPS-modulated DABC in [14]. A step-by-step closed-loop controller design is presented in this section.

By applying fundamental harmonic approximation (FHA) analysis [3], the fundamental components of v_{ab} and Nv_{cd} are expressed by (22) and (23), and hence the resonant current i_r

Authorized licensed use limited to: Macau Univ of Science and Technology. Downloaded on May 08,2025 at 08:12:51 UTC from IEEE Xplore. Restrictions apply.

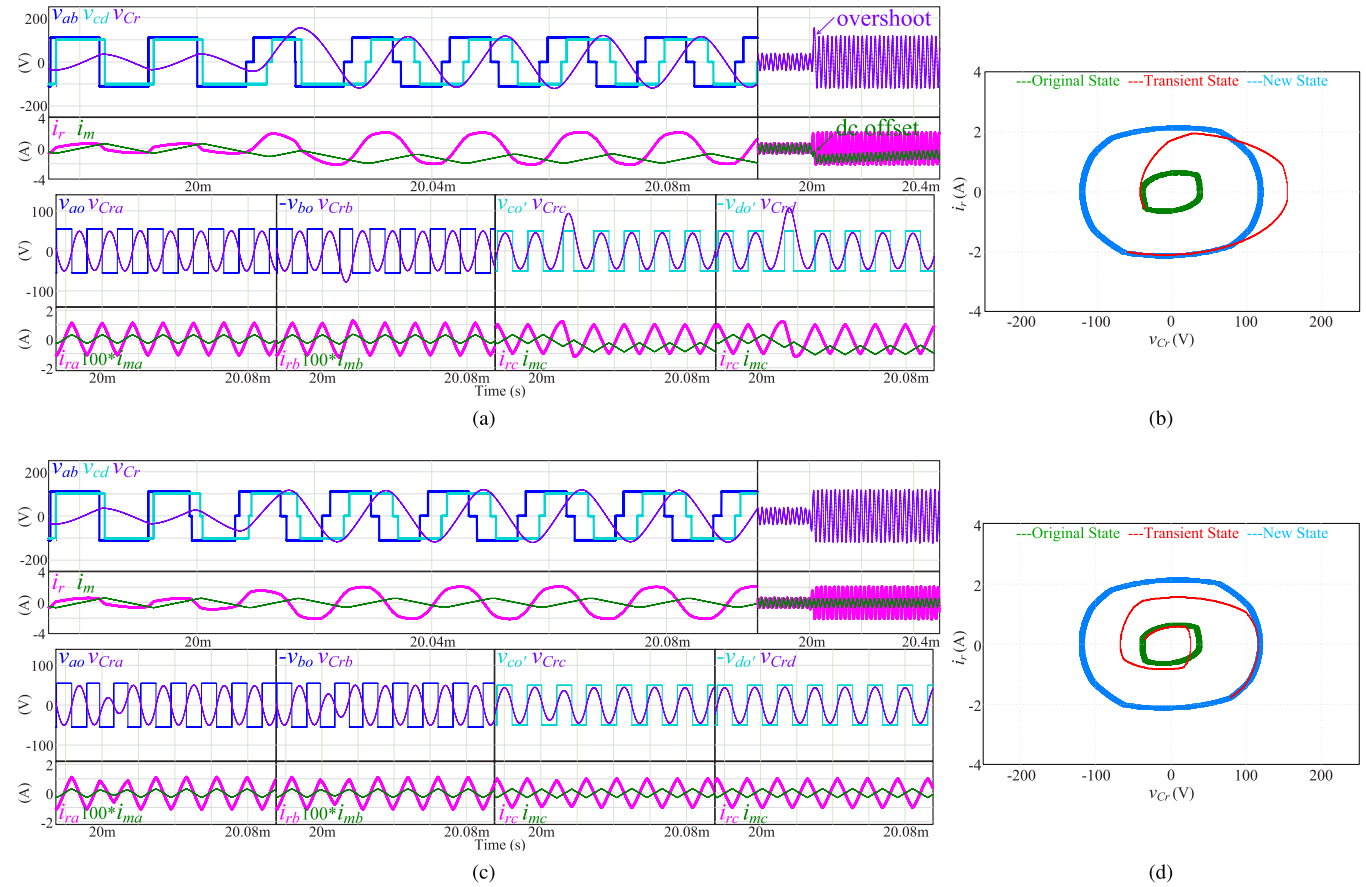

Fig. 6. Open-loop simulation examples from SPS mode to TPS mode under TSM [13] and GTSM with $V_1 = 110$ V, $V_2 = 100$ V, $f_s = 60$ kHz, and $F = 1.54$. Simulated transient waveforms under (a) TSM and (c) GTSM. v_{Cr}-i_r state-plane diagrams under (b) TSM and (d) GTSM.

can be approximated by (24)

$$v_{ab} \approx \frac{4V_1}{\pi} \cos\left[\frac{\theta_1}{2}\right] \sin\left[\omega_s t\right] \tag{22}$$

$$Nv_{cd} \approx \frac{4NV_2}{\pi} \cos\left[\frac{\theta_3}{2}\right] \sin\left[\omega_s t - \theta_2\right] \tag{23}$$

$$i_r \approx \frac{4V_1\left(M\cos\left[\frac{\theta_3}{2}\right]\cos\left[\omega_s t - \theta_2\right] - \cos\left[\frac{\theta_1}{2}\right]\cos\left[\omega_s t\right]\right)}{\pi X_r} \tag{24}$$

where $X_r = \omega_s L_r - 1/(\omega_s C_r)$ is the equivalent impedance and $M = NV_2/V_1$ is defined as the voltage gain of DABSRC. Next, the rms value of i_r, (i.e., i_{r_RMS}) and the output active power (i.e., P_o) can be calculated from (25) and (26), respectively

$$\begin{aligned} i_{r_\mathrm{RMS}} &= \sqrt{\frac{1}{T_s}\int_0^{T_s} i_r^2 \mathrm{d}t} \\ &= \frac{2\sqrt{2}V_1}{\pi X_r}\sqrt{\begin{array}{l}\cos^2\left[\frac{\theta_1}{2}\right] + M^2\cos^2\left[\frac{\theta_3}{2}\right] \\ -2M\cos\left[\frac{\theta_1}{2}\right]\cos\left[\frac{\theta_3}{2}\right]\cos\left[\theta_2\right]\end{array}} \\ P_o &= \frac{1}{T_s}\int_0^{T_s} v_{ab}\cdot i_r \mathrm{d}t \end{aligned} \tag{25}$$

$$= \frac{8NV_1V_2}{\pi^2 X_r}\sin\left[\theta_2\right]\cos\left[\frac{\theta_1}{2}\right]\cos\left[\frac{\theta_3}{2}\right]. \tag{26}$$

Typically, in order to maintain a high efficiency during steady state, i_{r_RMS} will be selected as the main optimization objective in DABSRC for minimizing conduction loss. The optimal steady-state phase-shift angles can be obtained by solving the constrained minimization problem (27) using the method of Lagrange multipliers [9]

$$\begin{aligned} &\underset{\theta_1,\theta_2,\theta_3}{\text{minimize}} \quad i_{r_\mathrm{RMS}}(\theta_1,\theta_2,\theta_3) \\ &\text{subject to} \quad P_o(\theta_1,\theta_2,\theta_3) = P_{o_d}, |P_{o_d}| \le P_{o_\max} \end{aligned} \tag{27}$$

where P_{o_d} is defined as the desired steady-state output power, and $P_{o_\max} = 8NV_1V_2/(\pi^2 X_r)$ is the theoretical maximum transmission power. Although the solution sets of (27) can be found in [9] and [16], the solution procedure is not accessible, and the results given in [16] contain some errors. Thus, in the Appendix, we provide the details of the solution procedure to find the optimal θ_1, θ_2, and θ_3 for achieving a minimum i_{r_RMS}. The optimal solution sets can be rewritten as follows: For Case 1 ($M > 1$ and $|P_{o_n}| \le \sqrt{1 - 1/(M^2)}$), (28) is valid; for Case 2 ($M < 1$ and $|P_{o_n}| \le \sqrt{1 - M^2}$), (29) is valid; for Case 3 (other operating regions), (30) is valid. Please note that

Authorized licensed use limited to: Macau Univ of Science and Technology. Downloaded on May 08,2025 at 08:12:51 UTC from IEEE Xplore. Restrictions apply.

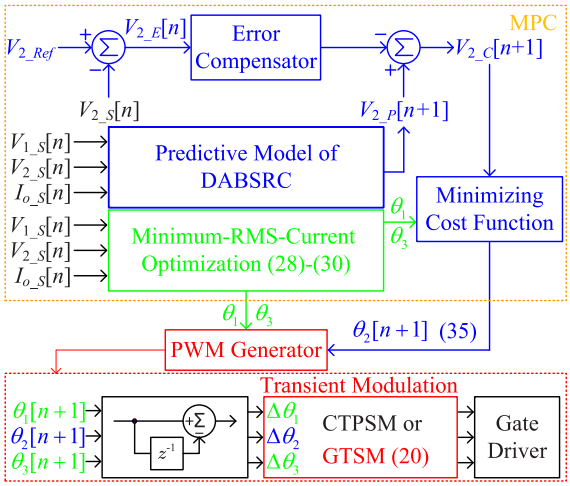

Fig. 7. Block diagram of MPC with minimum-rms-current optimization.

$P_{o_n} = P_{o_d}/P_{o_\max}$ is defined as the normalized output power

$$\begin{cases} \theta_1 = 0 \\ \theta_2 = \arctan\left[P_{o_n} \cdot M\right] \\ \theta_3 = 2\arccos\left[\sqrt{1/(M^2) + P_{o_n}^2}\right] \end{cases} \tag{28}$$

$$\begin{cases} \theta_1 = 2\arccos\left[\sqrt{M^2 + P_{o_n}^2}\right] \\ \theta_2 = \arctan\left[P_{o_n}/M\right] \\ \theta_3 = 0 \end{cases} \tag{29}$$

$$\begin{cases} \theta_1 = 0 \\ \theta_2 = \arcsin\left[P_{o_n}\right] \\ \theta_3 = 0. \end{cases} \tag{30}$$

Nevertheless, it should be highlighted that the expressions of optimal θ_1, θ_2, and θ_3 given by (28)–(30) cannot be directly used to form a closed-loop controller as they are steady-state solutions. A simple control scheme for MPS-modulated DABSRC used in this article is depicted in Fig. 7. With this control scheme, V_{2_Ref} is defined as the reference output voltage; $V_{1_S}[n]$, $V_{2_S}[n]$, and $I_{o_S}[n]$ are the sampled values of V_1, V_2, and I_o obtained via a 12-bit analog-to-digital converters (ADCs); $V_{2_P}[n+1]$ is the predicted output voltage for the next, i.e., $(n+1)$th, cycle; $V_{2_E}[n]$ is the error/deviation between the output voltage and its reference; $V_{2_C}[n+1]$ is defined as the predicted output voltage after correction. A standard quadratic cost function $\mathcal{J}$ of MPC is given by

$$\mathcal{J} = \left(V_{2_Ref} - V_{2_C}[n+1]\right)^2. \tag{31}$$

When implementing the control loop, the outer phase-shift angle θ_2 is computed to find a cost-minimizing control strategy, while the inner phase-shift angles θ_1 and θ_3 are directly determined using (28)–(30).

In general, the predictive model of DABSRC is established based on the average power model, i.e., (26), from which the dynamics of V_2 can be obtained as

$$C_o\frac{\mathrm{d}V_2}{\mathrm{d}t} = \frac{P_o}{V_2} - I_o$$

$$= \frac{8NV_1}{\pi^2 X_r}\sin\left[\theta_2\right]\cos\left[\frac{\theta_1}{2}\right]\cos\left[\frac{\theta_3}{2}\right] - I_o \tag{32}$$

where C_o is the total output capacitance. $V_{2_P}[n+1]$ can be obtained by discretizing (32) using the forward Euler method, which results in

$$V_{2_P}[n+1] = V_{2_S}[n] + \frac{\mathrm{d}V_{2_S}[n]}{\mathrm{d}t}T_s$$

$$= V_{2_S}[n] + \frac{8NV_{1_S}[n]\sin\theta_2\cos\frac{\theta_1}{2}\cos\frac{\theta_3}{2}}{\pi^2 X_r C_o f_s} - \frac{I_{o_S}[n]}{C_o f_s}. \tag{33}$$

Generally, in order to compensate for the unmodeled effects, a proportional–integral (PI) compensator should be used, and the compensator's output is added to $V_{2_P}[n+1]$ to produce $V_{2_C}[n+1]$. Thus,

$$V_{2_C}[n+1] = V_{2_P}[n+1] - \left(K_p V_{2_E}[n] + K_i\sum_{\tau=0}^{n} V_{2_E}[\tau]\right) \tag{34}$$

where K_p and K_i are, respectively, the proportional and integral gains to be designed, and $V_{2_E}[n] = V_{2_Ref} - V_{2_S}[n]$. Finally, minimizing $\mathcal{J}$, i.e., $\bigtriangledown\mathcal{J} = 0$, yields the predicted optimal outer phase-shift angle (or control variable)

$$\theta_2[n+1] = \arcsin\left[\frac{\pi^2 X_r C_o f_s}{8NV_{1_S}[n]\cos\frac{\theta_1}{2}\cos\frac{\theta_3}{2}}\left(\frac{I_{o_S}[n]}{C_o f_s} + K_p^* V_{2_E}[n] + K_i\sum_{\tau=0}^{n} V_{2_E}[\tau]\right)\right] \tag{35}$$

where $K_p^* = K_p + 1$ is the equivalent proportional gain. Evidently, the dynamics of DABSRC are affected by the choices of K_p^* and K_i. In general, larger values of K_p^* and K_i lead to higher closed-loop bandwidth and hence faster dynamic response.

As depicted in Fig. 7, the output voltage of DABSRC can be regulated by the MPC designed above with minimum-rms-current operation, while the PWM generator will receive its input from the controller and determine the strategy to update $\Delta\theta_1$, $\Delta\theta_2$, and $\Delta\theta_3$ either by CTPSM or GTSM. Fig. 8 shows the simulated closed-loop transient waveforms under MPC+CTPSM and MPC+GTSM with 200-Hz pulsed-power loads, where the load current periodically changes between 0.5 and 2.0 A. Other key specifications are given as follows: $V_1 = 125$ V, $V_2 = 100$ V, $C_o = 47$ μF, $f_s = 50$ kHz, $F = 1.2835$, and the PI control parameters are $K_p^* = 0.08$ and $K_i = 0.00008$. It can be seen that the overshoots and undershoots in i_r, v_{Cr}, and i_m under MPC+CTPSM are significantly larger than those under MPC+GTSM, and smoother transient waveforms are achieved under MPC+GTSM. The simulation results clearly demonstrate that transient oscillations, dc offsets, settling times of i_r, v_{Cr}, and i_m can be significantly minimized by GTSM, thus contributing positively to improving the dynamics of DABSRC.

V. Online Estimation of Resonant Frequency

Due to aging effects, environmental conditions (e.g., temperature and humidity), manufacturing tolerances, etc., the actual

Authorized licensed use limited to: Macau Univ of Science and Technology. Downloaded on May 08,2025 at 08:12:51 UTC from IEEE Xplore. Restrictions apply.

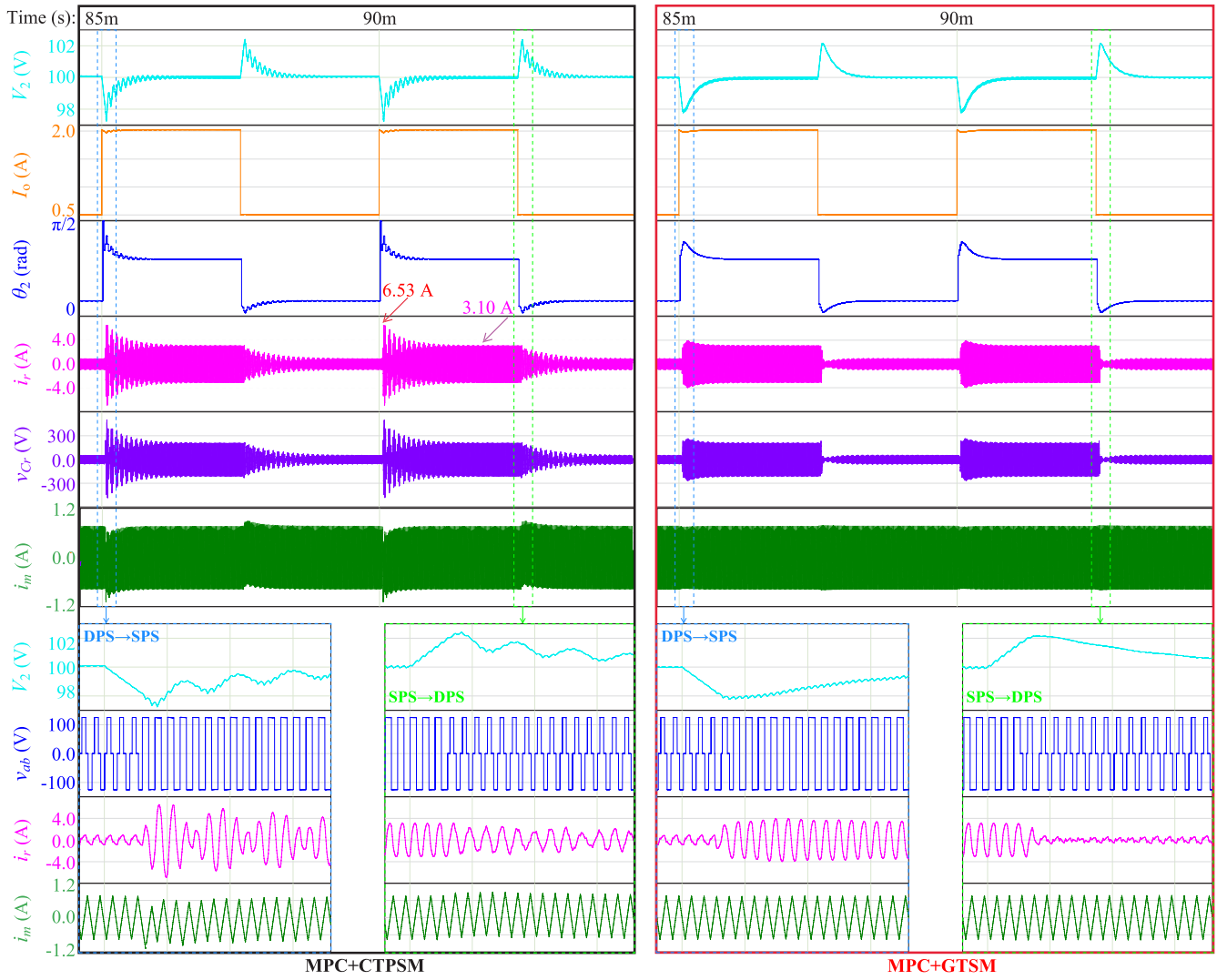

Fig. 8. Simulated closed-loop transient waveforms under 200-Hz 0.5-to-2-A pulsed-power loads. $V_1 = 125$ V, $V_2 = 100$ V, $f_s = 50$ kHz, $F = 1.2835$, $K_p^* = 0.08$, and $K_i = 0.00008$.

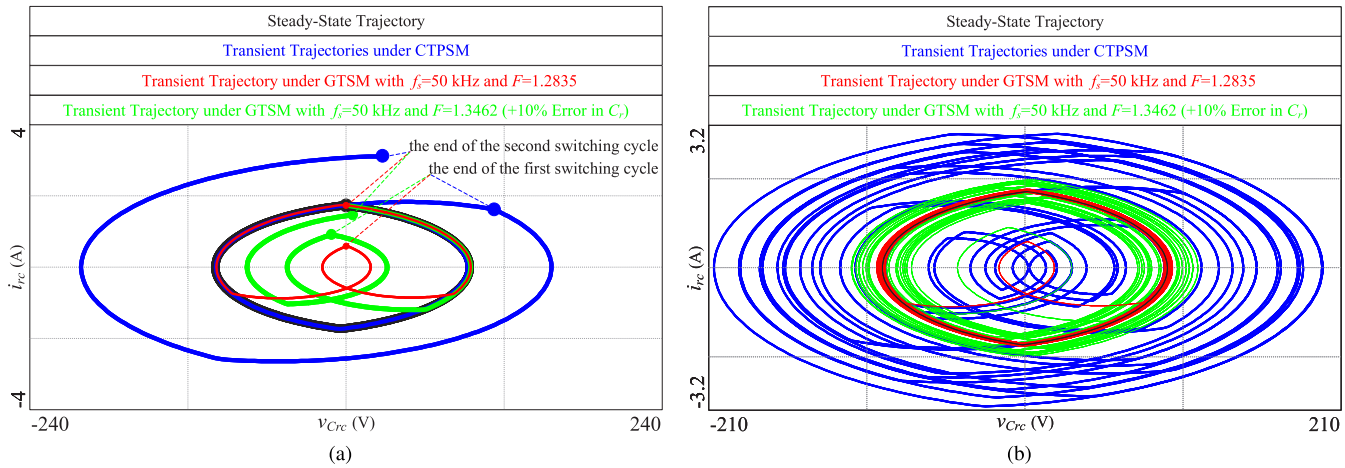

Fig. 9. Simulated transient v_{Crc}-i_{rc} state-plane diagrams in submodel 3 under open-loop conditions, where $\Delta\theta_3 = \pi/3$ (i.e., $\Delta\theta_{CD} = \pi/3$), $f_s = 50$ kHz, and $F = 1.2835$ (nominal value) or $F = 1.3462$ (+10% error in C_r). (a) Transient v_{Crc}-i_{rc} state-plane diagrams of the first two switching cycles. (b) Transient v_{Crc}-i_{rc} state-plane diagrams of 25 switching cycles.

Authorized licensed use limited to: Macau Univ of Science and Technology. Downloaded on May 08,2025 at 08:12:51 UTC from IEEE Xplore. Restrictions apply.

values of C_r and L_r may deviate from their nominal values, which can result in deviation in the resonant frequency f_r of DABSRC. It can be observed from (20) and (35) that both algorithms of GTSM and MPC are related to X_r and $F = f_s/f_r$, respectively. Thus, f_r is the most important converter parameter that determines both F and X_r. In most studies, f_r is regarded as having a constant value; nevertheless, in order to achieve the anticipated performance of the proposed GTSM, the effects of parameter deviations should not be ignored. To emulate the cases under resonant frequency deviations, the preset value of F in the GTSM program codes is modified, while the actual circuit parameters are kept unchanged.

Fig. 9 shows the simulated open-loop transient state-plane trajectories for $\Delta\theta_3 = \pi/3$ (or $\Delta\theta_{CD} = \pi/3$) in submodel 3 with $F = 1.2835$ (nominal value). If there exists a +10% error in the resonant capacitance C_r (i.e., $F = 1.3462$), the resulting error in transient pulsewidths will lead to small deviations from the desired transient trajectory (i.e., red curve), and the associated transient v_{Crc}-i_{rc} trajectory (i.e., green curve) can converge to the steady-state trajectory (i.e., black curve) within two switching cycles [see Fig. 9(a)]. As shown in Fig. 9(b), although the error in F leads to a certain degradation in performance, GTSM can still effectively suppress transient oscillations when compared to CTPSM. In addition, even with deviation in F, it can still effectively eliminate transient dc offsets in i_m, as (6) always holds. Thus, in general, although the performance of GTSM may degrade with a larger error in f_r or F, it still outperforms CTPSM in terms of transient performance.

Nevertheless, in the presence of significant deviations in X_r and F from the nominal values, the dynamic performance of closed-loop controlled DABSRC could be severely affected if its modulator and controller cannot adapt to changes in X_r and F. For this reason, an accurate value of f_r should be determined to achieve optimal dynamics in DABSRC. There are various automatic resonant-frequency tracking techniques proposed for this purpose [24], [25]. In this article, we adopted a simple perturb and observe (P&O) method, which is similar to that proposed in [26], to estimate X_r and F.

Neglecting all power losses,

$$P_o = V_2 \times I_o \tag{36}$$

and substituting (36) into (26) gives the estimation of X_r under TPS modulation

$$X_r = \frac{8NV_1}{\pi^2 I_o} \sin[\theta_2] \cos\left[\frac{\theta_1}{2}\right] \cos\left[\frac{\theta_3}{2}\right]. \tag{37}$$

In general, the exact values of C_r and L_r in a DABSRC may not be known but they can be treated as constant during the brief parameter identification process. As X_r changes with switching frequency f_s only, f_s must be perturbed to produce different values of X_r. In theory, for a given switching frequency f_{s_i}, its corresponding impedance X_{r_i} is given by

$$X_{r_i} = \sqrt{L_r/C_r}\,(F_i - 1/F_i) = Z_r\,(F_i - 1/F_i) \tag{38}$$

where $F_i = f_{s_i}/f_r$. Define the nominal impedance X_{r_n} as

$$X_{r_n} = \sqrt{L_r/C_r}\,(F_n - 1/F_n) = Z_r\,(F_n - 1/F_n) \tag{39}$$

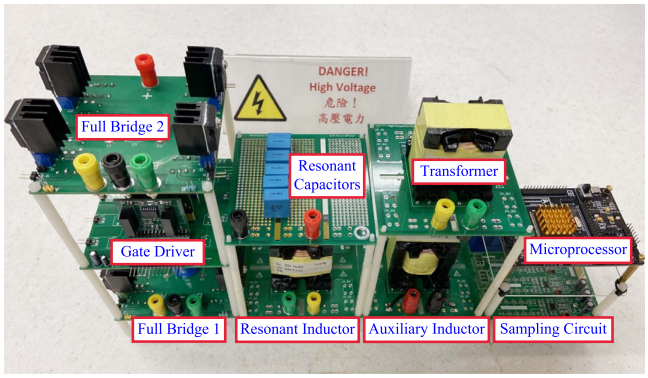

Fig. 10. Photograph of laboratory prototype of DABSRC.

where f_{s_n} is the nominal switching frequency, and hence $F_n = f_{s_n}/f_r$.

Combining (38) and (39), the estimated f_r and F (i.e., f_{r_e} and F_{n_e}) can be obtained from

$$f_{r_e} = \sqrt{\frac{X_{r_ie} f_{s_i} f_{s_n}^2 - X_{r_ne} f_{s_i}^2 f_{s_n}}{X_{r_ie} f_{s_i} - X_{r_ne} f_{s_n}}} \tag{40}$$

$$F_{n_e} = \sqrt{\frac{f_{s_n}\,(X_{r_ie} f_{s_i} - X_{r_ne} f_{s_n})}{f_{s_i}\,(X_{r_ie} f_{s_n} - X_{r_ne} f_{s_i})}}. \tag{41}$$

It should be emphasized that X_{r_ie} and X_{r_ne} used in (40) and (41) are the estimated values of X_{r_i} and X_{r_n} computed according to (37). By incorporating (37) and (41) into MPC and the proposed GTSM, respectively, the problems associated with parameter deviations can be mitigated. It should be noted that the accuracy of the parameter identification is affected by the accuracy of the power model of DABSRC, i.e., (26). As suggested by [26], a higher accuracy is achieved with SPS modulation. Thus, the parameter estimation algorithm is executed when DABSRC is operated with SPS modulation.

VI. Experimental Verification

As shown in Fig. 10, a scaled-down experimental prototype of DABSRC is constructed to validate the proposed GTSM. The circuit parameters used in the prototype are listed in Table III. The nominal switching frequency f_{s_n} in all experiments is set as 50 kHz (i.e., $F_n = 1.2835$ and $X_{r_n} = 39.6317$). In this article, we directly measure the magnetizing current through an auxiliary inductor, such that the measured current is $i_m/2$. It should be pointed out that the additional magnetizing inductance is much larger than the power transfer inductance L_r and the transformer's leakage inductance, and hence it has negligible influence on the performance of DABSRC. In addition, it is used only during the experimentation stage and can be omitted in practical implementation. The resonant capacitor C_r often needs to endure a high voltage in DABSRC, hence it is important to investigate the voltage stress of C_r. However, due to the limitations of oscilloscope channels, v_{Cr} is not directly measured in experiments as it generally has a similar profile as i_r.

Authorized licensed use limited to: Macau Univ of Science and Technology. Downloaded on May 08,2025 at 08:12:51 UTC from IEEE Xplore. Restrictions apply.

Fig. 11. Experimental open-loop transient waveforms with $V_1 = 110$ V, $V_2 = 100$ V, $f_s = 50$ kHz, and $F = 1.2835$. (a) Case I: Increasing power accompanied by a transition from TPS mode to DPS mode (i.e., $\theta_1 = 2\pi/15$, $\theta_2 = 11\pi/60$, $\theta_3 = \pi/10$, $\Delta\theta_1 = \pi/15$, $\Delta\theta_2 = 11\pi/60$, and $\Delta\theta_3 = -\pi/10$). (b) Case II: Decreasing power accompanied by a transition from SPS mode to TPS mode (i.e., $\theta_1 = 0$, $\theta_2 = 7\pi/15$, $\theta_3 = 0$, $\Delta\theta_1 = 2\pi/15$, $\Delta\theta_2 = -\pi/6$, and $\Delta\theta_3 = \pi/5$). (c) Case III: Reversing power flow direction accompanied by a transition from DPS mode to SPS mode (i.e., $\theta_1 = 0$, $\theta_2 = \pi/4$, $\theta_3 = \pi/10$, $\Delta\theta_1 = 0$, $\Delta\theta_2 = -23\pi/60$, and $\Delta\theta_3 = -\pi/10$).

As our work represents the first attempt to discourse the role of optimized transient modulation strategy in achieving high-quality dynamic response in MPS-modulated DABSRC, the proposed GTSM is merely compared with CTPSM in all experimental test cases.

A. Open-Loop Tests

In open-loop tests, both the input and output terminals of DABSRC are connected with dc voltage sources, which provides an ideal test environment equivalent to an infinite control bandwidth for evaluating the theoretical performances of CTPSM and GTSM. Both transient modulation strategies are executed only once with predefined $\Delta\theta_1$, $\Delta\theta_2$, and $\Delta\theta_3$.

Three open-loop transition cases, i.e., increasing power (Case I), decreasing power (Case II), and reversing power flow direction (Case III) are demonstrated in detail. It can be seen from Fig. 11 that GTSM can simultaneously mitigate transient oscillations and dc offsets in all cases. The maximum overshoots in i_r and i_m are reduced by 50% to 100% with GTSM, thus

Authorized licensed use limited to: Macau Univ of Science and Technology. Downloaded on May 08,2025 at 08:12:51 UTC from IEEE Xplore. Restrictions apply.

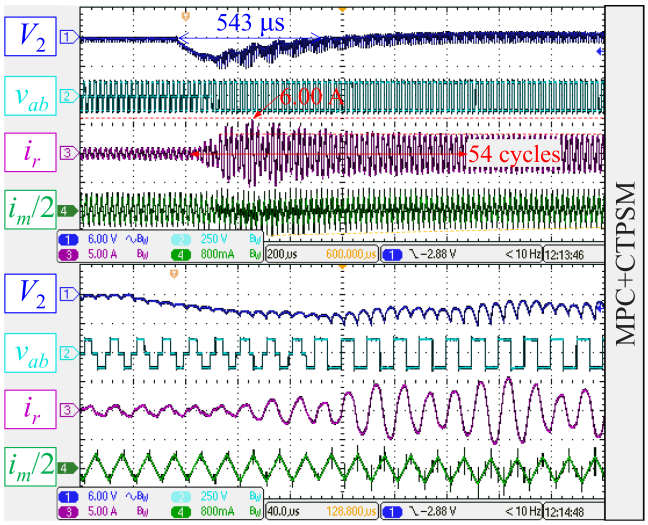

(a)

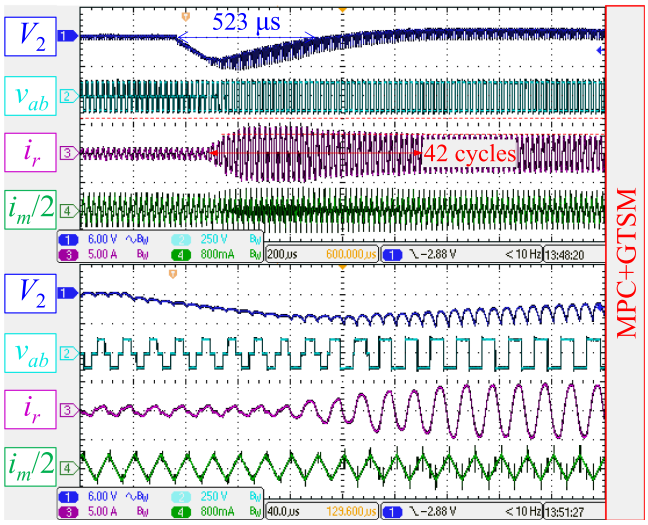

(b)

Fig. 12. Experimental closed-loop transient waveforms for a step-up load change from 0.5 to 2 A with $\{K_p^* = 0.055,\ K_i = 0.0015\}$ under (a) MPC+CTPSM and (b) MPC+GTSM. $V_1 = 125$ V, $V_2 = 100$ V, $f_s = 50$ kHz, $F = 1.2835$, and $X_r = 39.6317$.

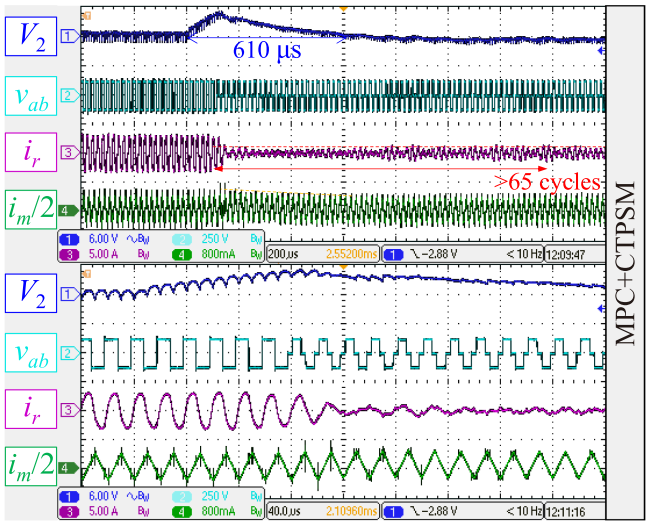

(a)

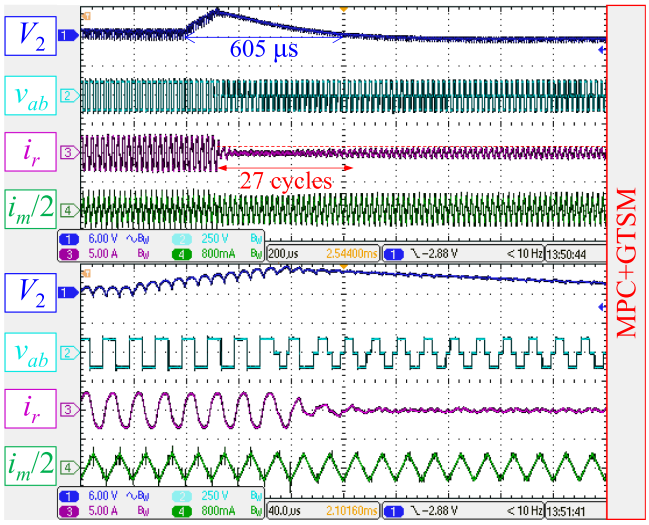

(b)

Fig. 13. Experimental closed-loop transient waveforms for a step-down load change from 2 to 0.5 A with $\{K_p^* = 0.055,\ K_i = 0.0015\}$ under (a) MPC+CTPSM and (b) MPC+GTSM. $V_1 = 125$ V, $V_2 = 100$ V, $f_s = 50$ kHz, $F = 1.2835$, and $X_r = 39.6317$.

minimizing transient voltage and current stresses on the power devices and ensuring smooth transient operation. GTSM also enables DABSRC to seamlessly reach the desired new steady state within a few switching cycles. The results shown in Fig. 11 also match with our theoretical analysis in Sections II and III as well as the findings from simulation results, which demonstrate the importance of effective transient modulation in optimizing the dynamic performance of DABSRC. In addition, although GTSM cannot guarantee transient ZVS, it enables DABSRC to reach the new steady state more rapidly and achieve steady-state ZVS instead. Thus, it can be found from Fig. 11 that, compared with GTSM, voltage spikes in v_{ab} and v_{cd} under CTPSM sustain for a longer period of time which could degrade the reliability of the power switches.

B. Closed-Loop Tests

In closed-loop tests, the output terminal is connected to a purely resistive load R_L, and the output voltage is regulated by the MPC designed in Section IV. All tests are conducted under large-amplitude step-load changes between 0.5 and 2.0 A. According to the analysis of minimum-rms-current operation, DABSRC should work under DPS mode at light load (i.e., 0.5 A) and SPS mode at heavy load (i.e., 2.0 A). Since the phase-shift angles are computed in real time under closed-loop conditions, both CTPSM and GTSM are implemented on a cycle-by-cycle basis. The update frequency of the PWM generator and sampling frequencies of ADCs are set as f_s, while the algorithm of MPC is executed every two switching cycles $(0.5/f_s)$. Three sets of control parameters (i.e., $\{K_p^* = 0.055, K_i = 0.0015\}$, $\{K_p^* = 0.08,$

Authorized licensed use limited to: Macau Univ of Science and Technology. Downloaded on May 08,2025 at 08:12:51 UTC from IEEE Xplore. Restrictions apply.

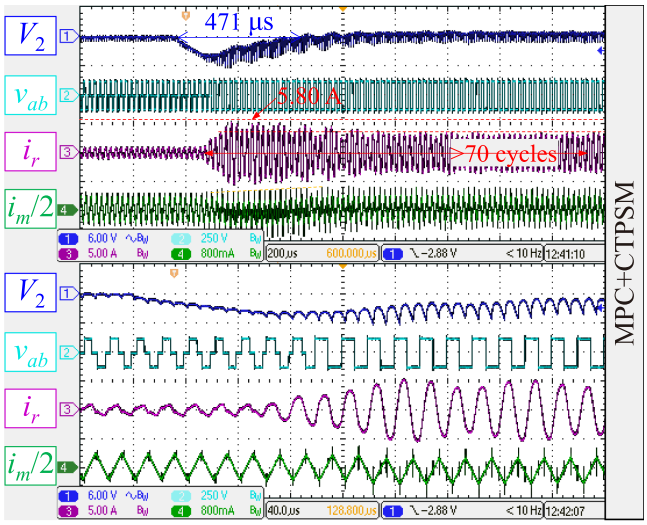

(a)

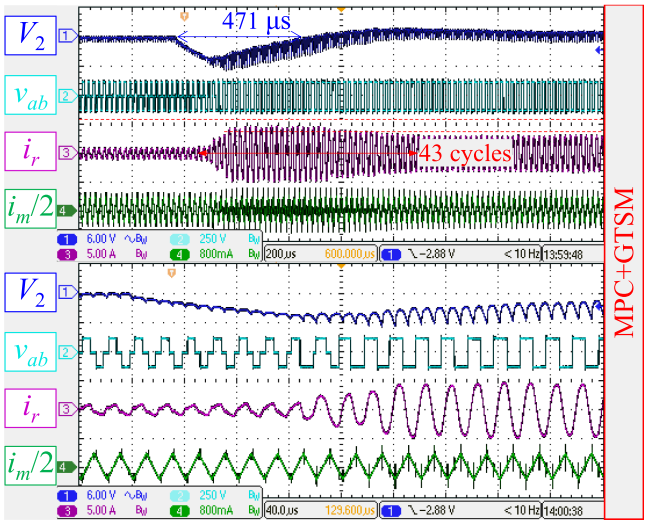

(b)

Fig. 14. Experimental closed-loop transient waveforms for a step-up load change from 0.5 to 2 A with $\{K_p^* = 0.08,\ K_i = 0.002\}$ under (a) MPC+CTPSM and (b) MPC+GTSM. $V_1 = 125$ V, $V_2 = 100$ V, $f_s = 50$ kHz, $F = 1.2835$, and $X_r = 39.6317$.

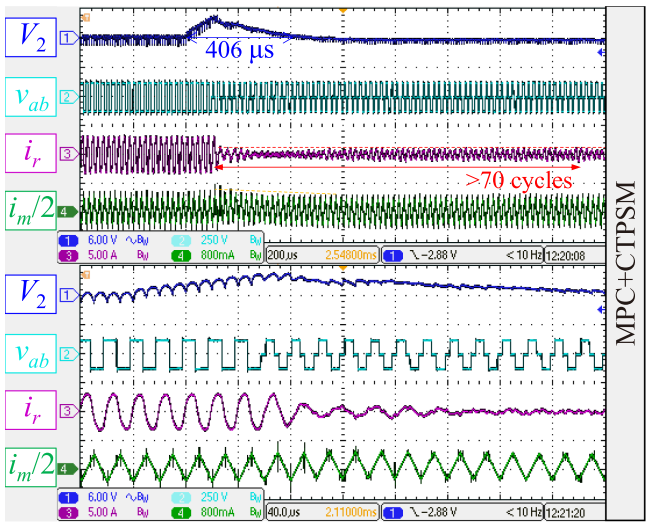

(a)

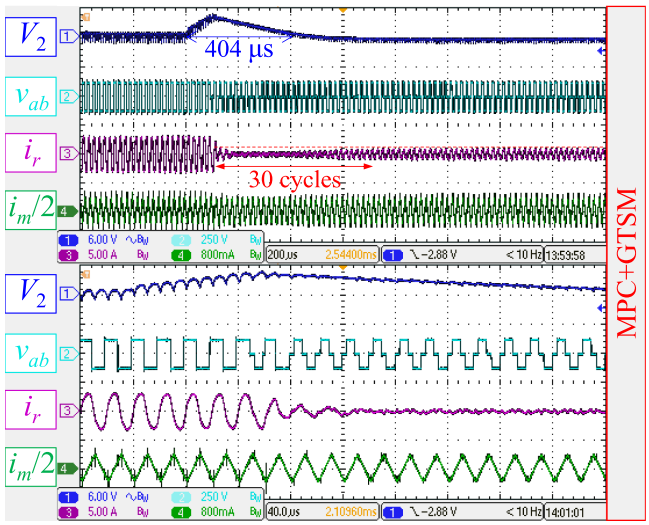

(b)

Fig. 15. Experimental closed-loop transient waveforms for a step-down load change from 2 to 0.5 A with $\{K_p^* = 0.08,\ K_i = 0.002\}$ under (a) MPC+CTPSM and (b) MPC+GTSM. $V_1 = 125$ V, $V_2 = 100$ V, $f_s = 50$ kHz, $F = 1.2835$, and $X_r = 39.6317$.

$K_i = 0.002\}$, and $\{K_p^* = 0.15,\ K_i = 0.004\}$) are selected to comprehensively compare the transient performances of DAB-SRC under MPC+CTPSM and MPC+GTSM. The experimental closed-loop transient waveforms of DABSRC implemented with different control parameters are shown in Figs. 12–17.

As can be seen from the experimental results, the maximum voltage deviations under both MPC+CTPSM and MPC+GTSM with different control parameters do not differ significantly from each other as the voltage deviations are mainly determined by the value of the output capacitance. The recovery time of the output voltage generally decreases with increasing controller's bandwidth (i.e., K_p^*), but MPC+GTSM leads to shorter recovery time as compared with MPC+CTPSM. If we carefully examine the waveforms of i_r and i_m, the actual settling times of i_r and i_m increase with increasing controller's bandwidth under MPC+CTPSM. Moreover, as shown in Figs. 13(a) and 17(a), the output voltage under MPC+CTPSM continuously oscillates about the reference voltage for a relatively long time due to the inaccurate trajectory tracking caused by CTPSM. Compared with MPC+CTPSM, the settling times of both i_r and i_m can be significantly reduced by MPC+GTSM and they are not sensitive to the controller's bandwidth, as they can approach their new steady-state values rapidly without undergoing any transient oscillations and dc offsets. Another important observation is that MPC+CTPSM shows large-amplitude overshoots in both i_r and i_m especially under the cases of step-up load changes, and such issues become more severe with higher controller's bandwidth. On the contrary, the overshoots can be effectively suppressed by MPC+GTSM and do not change noticeably with different control parameters. Meanwhile, as the high-frequency resonant current is translated to the output current of DABSRC after rectification, the output voltage quality is much improved as

Authorized licensed use limited to: Macau Univ of Science and Technology. Downloaded on May 08,2025 at 08:12:51 UTC from IEEE Xplore. Restrictions apply.

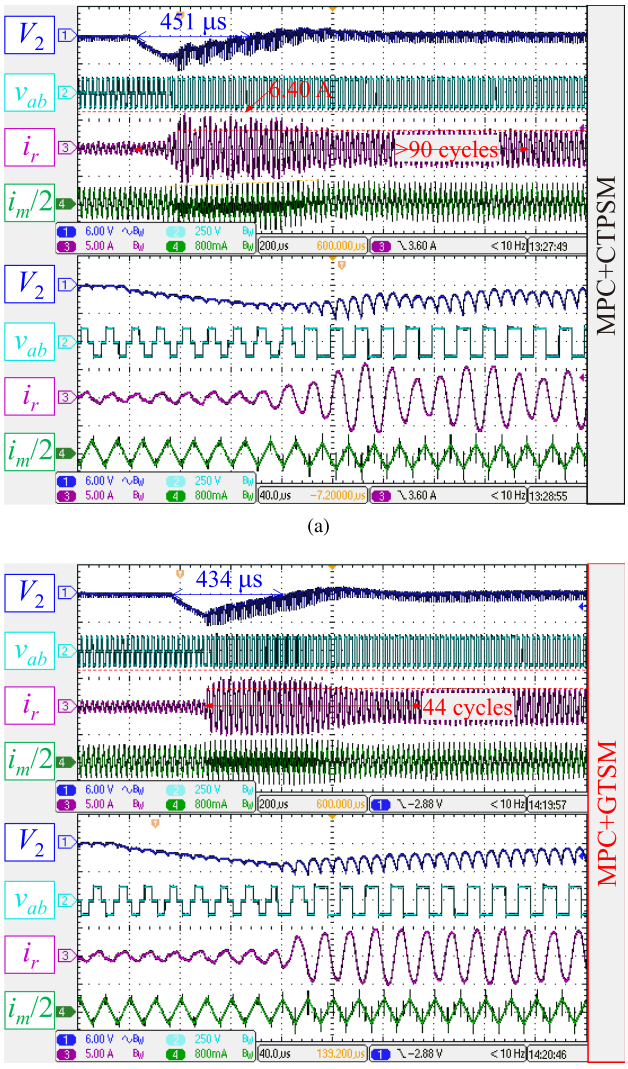

(a) (b)

Fig. 16. Experimental closed-loop transient waveforms for a step-up load change from 0.5 to 2 A with $\{K_p^* = 0.15,\ K_i = 0.004\}$ under (a) MPC+CTPSM and (b) MPC+GTSM. $V_1 = 125$ V, $V_2 = 100$ V, $f_s = 50$ kHz, $F = 1.2835$, and $X_r = 39.6317$.

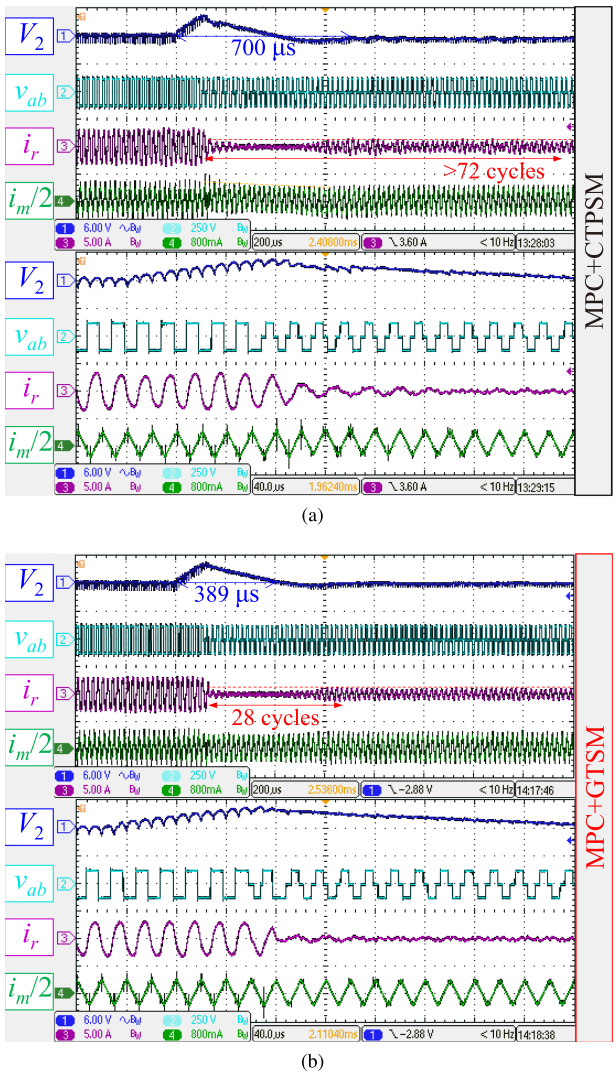

(a) (b)

Fig. 17. Experimental closed-loop transient waveforms for a step-down load change from 2 to 0.5 A with $\{K_p^* = 0.15,\ K_i = 0.004\}$ under (a) MPC+CTPSM and (b) MPC+GTSM. $V_1 = 125$ V, $V_2 = 100$ V, $f_s = 50$ kHz, $F = 1.2835$, and $X_r = 39.6317$.

a consequence under MPC+GTSM and does not suffer from any transient oscillations. These experimental results also agree well with the closed-loop simulation results shown in Fig. 8. Overall, the quality of DABSRC's waveforms deteriorates with increasing controller's bandwidth under MPC+CTPSM, while they are consistently maintained at high quality under MPC+GTSM. It can therefore be safely concluded that GTSM is more compatible with high-gain, high-bandwidth, and fast controller due to its ability to drive DABSRC to new steady state swiftly with no transient oscillations and dc bias.

C. Parameter Sensitivity Tests

To ensure a meaningful parameter sensitivity test, the initial values of X_r and F in the program codes of MPC and GTSM are deliberately set to some incorrect values, and the DABSRC is constantly operated under SPS mode.

Fig. 18 shows the open-loop transient experiments with CTPSM and GTSM considering the presence of errors in the resonant capacitance. It is apparent that if the capacitance error is no more than 20%, GTSM can still effectively suppress the transient oscillations and overshoots in i_r. Even if the capacitance error increases to 50%, GTSM still achieves a better transient performance over CTPSM. In addition, the transient dc offset in i_m is effectively eliminated by GTSM in all cases. Thus, it can be concluded that GTSM is inherently not sensitive to parameter deviations.

Fig. 19 illustrates the experimental online estimation of X_r and F under closed-loop conditions. The changes in X_r are monitored through a digital-to-analog converter (DAC) module and can be observed from Channel 2's waveforms. The initial (incorrect) values of X_r and F are set as 49.8339 and 1.4060, respectively, which deviate from the nominal values ($X_{r_n} = 39.6317$ and $F_n = 1.2835$). Before T_1, the converter works with

Authorized licensed use limited to: Macau Univ of Science and Technology. Downloaded on May 08,2025 at 08:12:51 UTC from IEEE Xplore. Restrictions apply.

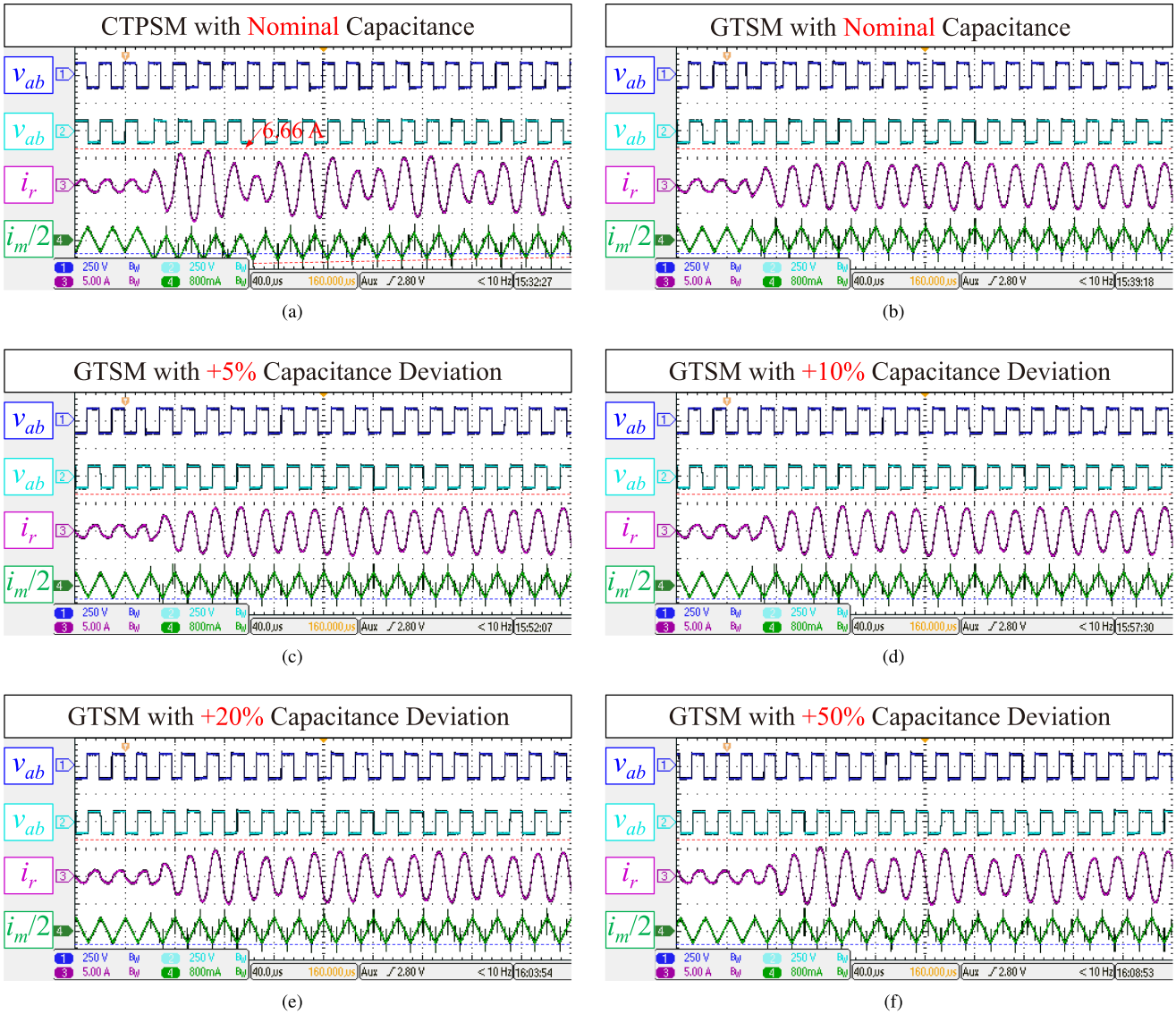

Fig. 18. Experimental open-loop transient waveforms under CTPSM and GTSM while considering different capacitance errors. $V_1 = 110$ V, $V_2 = 100$ V, $f_s = 50$ kHz, $\theta_1 = \Delta\theta_1 = 0$, $\theta_3 = \Delta\theta_3 = 0$, $\theta_2 = \pi/9$, and $\Delta\theta_2 = 4\pi/9$. (a) CTPSM with nominal capacitance (i.e., $F = 1.2835$). (b) GTSM with nominal capacitance. (c) GTSM with +5% capacitance deviation (i.e., $F = 1.3152$). (d) GTSM with +10% capacitance deviation (i.e., $F = 1.3462$). (e) GTSM with +20% capacitance deviation (i.e., $F = 1.4060$). (f) GTSM with +50% capacitance deviation (i.e., $F = 1.5720$).

incorrect X_r and F at a light load. At T_1, the load is suddenly changed, and the converter operates at a heavy load. By zooming in the waveforms around T_1, it can be found that even with the incorrect X_r and F, the transient oscillations and overshoots in i_r under MPC+GTSM are much smaller than those under MPC+CTPSM. At T_2, the system has reached the steady state, and the switching frequency will gradually increase to f_{s_i} from f_{s_n} until T_3. The online estimation of X_{r_i} starts from T_3 and will last until T_4, and the estimated values are recorded every two switching cycles. After data processing, the average value of X_{r_i}, i.e., X_{r_ie} can be obtained, which is regarded as the estimated value of X_{r_i} corresponding to f_{s_i}. From T_4, the switching frequency is gradually restored to the nominal value f_{s_n} until T_5. From T_5 to T_6, online estimation restarts, and the estimated impedance X_{r_ne} corresponding to f_{s_n} can be obtained similarly as X_{r_ie}. With X_{r_ie} and X_{r_ne} available, the estimated nominal value of F (i.e., F_{n_e}) can be calculated from (41) accordingly. At T_6, the estimated values of X_{r_ne} and F_{n_e} are incorporated into MPC and GTSM, and the execution of parameter estimation comes to an end. The values of X_{r_ne} under MPC+CTPSM and MPC+GTSM are 40.59 and 40.26, respectively, which are close to the actual nominal value $X_{r_n} = 39.6317$. To verify the dynamics after correction of X_r and F, a step-down load transient is initiated at T_7, followed by a step-up load transient at T_8. As can be seen from the zoomed-in transient waveforms around T_7 and T_8, similar to the results reported in Section VI-B, MPC+GTSM always shows a significantly better transient performance over MPC+CTPSM. In addition, for the cases of step-up load transients, the maximum overshoots at T_8 under both MPC+CTPSM and MPC+GTSM are reduced

Authorized licensed use limited to: Macau Univ of Science and Technology. Downloaded on May 08,2025 at 08:12:51 UTC from IEEE Xplore. Restrictions apply.

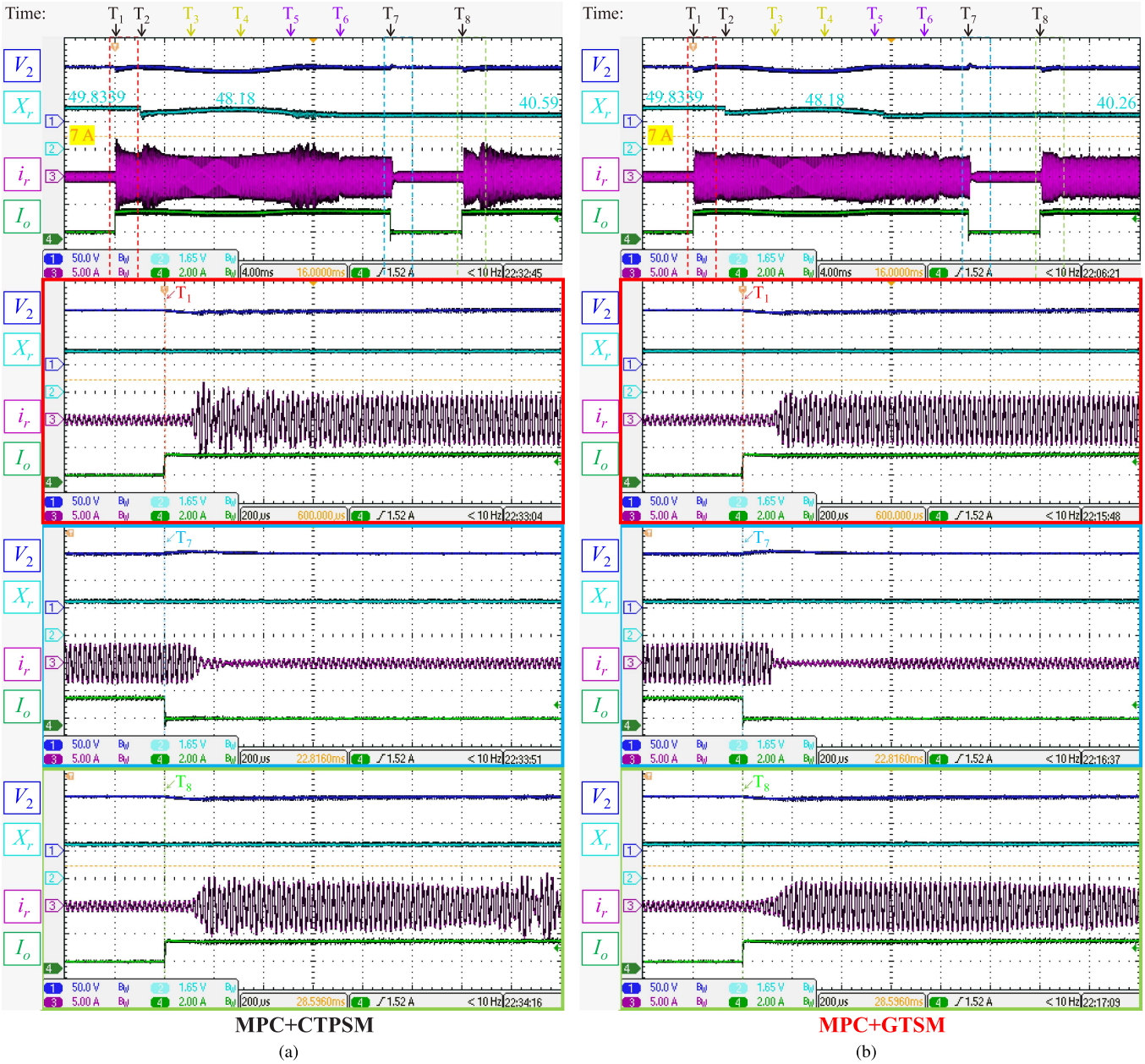

Fig. 19. Experimental closed-loop online estimation of X_r and F. Transient waveforms for step load changes between 0.5 and 2 A are shown under (a) MPC+CTPSM and (b) MPC+GTSM. $V_1 = 110$ V, $V_2 = 100$ V, $K_p^* = 0.08$, $K_i = 0.002$, $f_{s_n} = 50$ kHz, $f_{s_i} = 52$ kHz, initial (incorrect) values of $X_r = 49.8339$ and $F = 1.4060$.

compared to those at T_1, which demonstrates the effectiveness of the online parameter estimation procedure.

VII. Conclusion

In summary, this study confirms the suitability of state-plane-trajectory-based modulation strategies for regulating the energy state of the resonant tank of DABSRC. The proposed GTSM represents the first method that can realize the stated objective, i.e., fast, oscillation-free, and dc-offset-free transition from old to new steady state in MPS-modulated DABSRC. In addition, the proposed algorithm of GTSM is sensorless, formulated in analytical form, and insensitive to deviations in resonant tank's parameters, which facilitates its real-time closed-loop implementation in practical applications. Both open-loop and closed-loop test results demonstrate the superior performance of GTSM over CTPSM. When combined with advanced control algorithm, such as MPC, which requires fast settling time on a cycle-by-cycle basis in order to deliver the anticipated performance, the proposed GTSM represents a much more effective method compared to CTPSM in terms of achieving fast and smooth (transient oscillation-free and dc-offset-free) responses to extremely fast control actions commanded by MPC or other advanced control algorithms.

Authorized licensed use limited to: Macau Univ of Science and Technology. Downloaded on May 08,2025 at 08:12:51 UTC from IEEE Xplore. Restrictions apply.

APPENDIX
SOLUTION PROCEDURE FOR (27)

The constrained optimization problem in (27) is often solved by using the Lagrange multipliers, and the procedure can be divided into three main steps.

Step 1: A Lagrangian function is constructed as follows:

$$\mathcal{L}(\theta_1, \theta_2, \theta_3, \lambda) = i_{r_\text{RMS}} + \lambda(P_o - P_{o_d}) \quad \text{(A.1)}$$

where variable $\lambda \neq 0$ is a Lagrange multiplier.

Step 2: Differentiating $\mathcal{L}$ with respect to θ_1, θ_2, θ_3, and λ, and equating the results to zero, we have

$$\nabla\mathcal{L}(\theta_1, \theta_2, \theta_3, \lambda) = 0. \quad \text{(A.2)}$$

Step 3: By solving (A.2), we can obtain the four equations corresponding to $\partial_{\theta_1}\mathcal{L} = 0$, $\partial_{\theta_2}\mathcal{L} = 0$, $\partial_{\theta_3}\mathcal{L} = 0$, and $\partial_{\lambda}\mathcal{L} = 0$. If $\theta_1 \neq \pi$ and $\theta_3 \neq \pi$, $\partial_{\theta_2}\mathcal{L} = 0$ leads to (A.3), and λ can be found accordingly

$$\frac{\pi \tan\theta_2}{2\lambda V_1} = \sqrt{\begin{aligned}&1 + \cos\theta_1 + M^2(1 + \cos\theta_3)\\ &- 4M\cos\tfrac{\theta_1}{2}\cos\theta_2\cos\tfrac{\theta_3}{2}.\end{aligned}} \quad \text{(A.3)}$$

Substituting (A.3) into $\partial_{\theta_1}\mathcal{L} = 0$ and $\partial_{\theta_3}\mathcal{L} = 0$, and then simplifying the results yields (A.4) and (A.5), respectively

$$\sin\frac{\theta_1}{2}\left[\cos\frac{\theta_1}{2}\cot\theta_2 - M\cos\frac{\theta_3}{2}\csc\theta_2\right] = 0 \quad \text{(A.4)}$$

$$\sin\frac{\theta_3}{2}\left[M\cos\frac{\theta_3}{2}\cot\theta_2 - \cos\frac{\theta_1}{2}\csc\theta_2\right] = 0. \quad \text{(A.5)}$$

In addition, $\partial_{\lambda}\mathcal{L} = 0$ gives $P_o = P_{o_d}$, and hence

$$P_{o_n} = \frac{P_{o_d}}{P_{o_\max}} = \cos\frac{\theta_1}{2}\cos\frac{\theta_3}{2}\sin\theta_2. \quad \text{(A.6)}$$

We now have three cases to simultaneously satisfy (A.4), (A.5), and (A.6).

Case 1: If $\theta_1 = 0$ and $\theta_3 \neq 0$, (A.4) always holds, and (A.5) and (A.6) can be simplified to (A.7) and (A.8), respectively

$$M\cos\frac{\theta_3}{2}\cos\theta_2 = 1 \quad \text{(A.7)}$$

$$P_{o_n} = \cos\frac{\theta_3}{2}\sin\theta_2. \quad \text{(A.8)}$$

Thus, we can obtain (28) by solving (A.7) and (A.8). It is apparent from (A.7) that (28) only exists when $M > 1$. In addition, as the range of validity of inverse cosine function (arccos) is limited to $[-1, 1]$, the solution of θ_3 in (28) is valid only when $|P_{o_n}| \leq \sqrt{1 - 1/(M^2)}$. In fact, if $|P_{o_n}| > \sqrt{1 - 1/(M^2)}$, θ_3 will approach zero.

Case 2: If $\theta_1 \neq 0$ and $\theta_3 = 0$, (A.5) always holds, and (A.4) and (A.6) can be simplified to (A.9) and (A.10), respectively

$$M = \cos\frac{\theta_1}{2}\cos\theta_2 \quad \text{(A.9)}$$

$$P_{o_n} = \cos\frac{\theta_1}{2}\sin\theta_2. \quad \text{(A.10)}$$

Similarly, we can obtain (29) by solving (A.9) and (A.10). According to (A.9) and the range of validity of arccos, (29) only exists when $M < 1$ and $|P_{o_n}| \leq \sqrt{1 - M^2}$. In addition, when $|P_{o_n}| > \sqrt{1 - M^2}$, θ_1 will approach zero.

Case 3: If $\theta_1 = 0$ and $\theta_3 = 0$, both (A.4) and (A.5) always hold, and (A.6) can be simplified to

$$P_{o_n} = \sin\theta_2 \quad \text{(A.11)}$$

which yields (30) applicable to the other cases not covered by Case 1 and Case 2.

REFERENCES

[1] R. De Doncker, D. Divan, and M. Kheraluwala, "A three-phase soft-switched high-power-density DC/DC converter for high-power applications," *IEEE Trans. Ind. Appl.*, vol. 27, no. 1, pp. 63–73, Jan./Feb. 1991.

[2] S. Inoue and H. Akagi, "A bidirectional isolated DC–DC converter as a core circuit of the next-generation medium-voltage power conversion system," *IEEE Trans. Power Electron.*, vol. 22, no. 2, pp. 535–542, Mar. 2007.

[3] X. Li and A. K. S. Bhat, "Analysis and design of high-frequency isolated dual-bridge series resonant DC/DC converter," *IEEE Trans. Power Electron.*, vol. 25, no. 4, pp. 850–862, Apr. 2010.

[4] G. Liu, Y. Jang, M. M. Jovanović, and J. Q. Zhang, "Implementation of a 3.3-kW DC–DC converter for EV on-board charger employing the series-resonant converter with reduced-frequency-range control," *IEEE Trans. Power Electron.*, vol. 32, no. 6, pp. 4168–4184, Jun. 2017.

[5] F. Krismer, J. Biela, and J. Kolar, "A comparative evaluation of isolated bi-directional dc/dc converters with wide input and output voltage range," in *Proc. 14th IAS Annu. Meeting. Conf. Rec. Ind. Appl. Conf.*, 2005, pp. 599–606.

[6] G. Ortiz, J. Biela, D. Bortis, and J. W. Kolar, "1 megawatt, 20 kHz, isolated, bidirectional 12 kV to 1.2 kV DC-DC converter for renewable energy applications," in *Proc. Int. Power Electron. Conf.*, 2010, pp. 3212–3219.

[7] R. Lenke, F. Mura, and R. W. De Doncker, "Comparison of non-resonant and super-resonant dual-active ZVS-operated high-power DC-DC converters," in *Proc. 13th Eur. Conf. Power Electron. Appl.*, 2009, pp. 1–10.

[8] J. Wu, Y. Li, X. Sun, and F. Liu, "A new dual-bridge series resonant DC–DC converter with dual tank," IEEE Trans. Power Electron., vol. 33, no. 5, pp. 3884–3897, May 2018.

[9] L. Corradini, D. Seltzer, D. Bloomquist, R. Zane, D. Maksimović, and B. Jacobson, "Minimum current operation of bidirectional dual-bridge series resonant DC/DC converters," *IEEE Trans. Power Electron.*, vol. 27, no. 7, pp. 3266–3276, Jul. 2012.

[10] G. Chen, X. Li, and S. Zhou, "Unified boundary control with phase shift compensation for dual bridge series resonant DC-DC converter," *IEEE Access*, vol. 8, pp. 131137–131149, 2020.

[11] J. Wu, W. Zhang, X. Sun, and X. Su, "Research on reactive power optimization control of a series-resonant dual-active-bridge converter," *Energies*, vol. 15, no. 11, 2022, Art. no. 3856.

[12] S. S. Chakraborty and K. Hatua, "Modeling with beat frequency dynamics and phase-frequency control design for a dual-bridge series resonant converter," IEEE Trans. Ind. Electron., vol. 69, no. 8, pp. 7952–7962, Aug. 2022.

[13] C. Sun, X. Jiang, L. Cao, and K. H. Loo, "Total suppression of high-frequency transient oscillations in dual-active-bridge series-resonant converter by trajectory-switching modulation," *IEEE Trans. Power Electron.*, vol. 37, no. 6, pp. 6511–6529, Jun. 2022.

[14] F. An, W. Song, B. Yu, and K. Yang, "Model predictive control with power self-balancing of the output parallel dab DC–DC converters in power electronic traction transformer," IEEE Trans. Emerg. Sel. Topics Power Electron., vol. 6, no. 4, pp. 1806–1818, Dec. 2018.

Authorized licensed use limited to: Macau Univ of Science and Technology. Downloaded on May 08,2025 at 08:12:51 UTC from IEEE Xplore. Restrictions apply.

[15] W. Song, M. Zhong, S. Luo, and S. Yang, "Model predictive power control for bidirectional series-resonant isolated DC–DC converters with fast dynamic response in locomotive traction system," *IEEE Trans. Transport. Electrific.*, vol. 6, no. 3, pp. 1326–1337, Sep. 2020.
[16] W. Song, M. Zhong, Y. Deng, S. Yin, and B. Yu, "Model predictive power control for bidirectional series resonant isolated DC–DC converters with steady-state and dynamic performance optimization," *IEEE J. Emerg. Sel. Topics Ind. Electron.*, vol. 3, no. 3, pp. 604–615, Jul. 2022.
[17] R. Duan, L. Yuan, Q. Gu, J. Nie, and Z. Zhao, "Trajectory-prediction-based fast bidirectional power transient control for series resonant dual-active-bridge converter," in *Proc. IEEE Energy Convers. Congr. Expo.*, 2018, pp. 1415–1422.
[18] H. Xu, S.-Z. Zhou, X. Li, H. Chen, and S. Hu, "Fast transient modulation of a dual-bridge series resonant converter," in *Proc. IECON 47th Annu. Conf. IEEE Ind. Electron. Soc.*, 2021, pp. 1–6.
[19] R. W. T. Bonten, J. M. Schellekens, B. J. D. Vermulst, F. M. Clermonts, and H. Huisman, "Improved dynamic behavior for the series-resonant converter using bidirectional charge control," *IEEE Trans. Power Electron.*, vol. 37, no. 10, pp. 11607–11619, Oct. 2022.
[20] J. Hu, S. Cui, D. v. d. Hoff, and R. W. De Doncker, "Generic dynamic phase-shift control for bidirectional dual-active bridge converters," *IEEE Trans. Power Electron.*, vol. 36, no. 6, pp. 6197–6202, Jun. 2021.
[21] C. Sun, X. Jiang, J. Liu, L. Cao, Y. Yang, and K. H. Loo, "A unified design approach of optimal transient single-phase-shift modulation for nonresonant dual-active-bridge converter with complete transient DC-offset elimination," *IEEE Trans. Power Electron.*, vol. 37, no. 11, pp. 13217–13237, Nov. 2022.
[22] C. Sun, X. Li, and S.-Z. Zhou, "Transient current control for a step load change in a dual-active-bridge converter," *Electron. Lett.*, vol. 54, no. 22, pp. 1290–1292, 2018.
[23] Q. Bu, H. Wen, J. Wen, Y. Hu, and Y. Du, "Transient DC bias elimination of dual-active-bridge DC–DC converter with improved triple-phase-shift control," *IEEE Trans. Ind. Electron.*, vol. 67, no. 10, pp. 8587–8598, Oct. 2020.
[24] J. Liu, G. Wang, G. Xu, J. Peng, and H. Jiang, "A parameter identification approach with primary-side measurement for DC–DC wireless-power-transfer converters with different resonant tank topologies," *IEEE Trans. Transport. Electrific.*, vol. 7, no. 3, pp. 1219–1235, Sep. 2021.
[25] Y. Wei, Q. Luo, and H. A. Mantooth, "A resonant frequency tracking technique for LLC converter-based DC transformers," *IEEE J. Emerg. Sel. Topics Ind. Electron.*, vol. 2, no. 4, pp. 579–590, Oct. 2021.
[26] Z. Guo, Y. Luo, and K. Sun, "Parameter identification of the series inductance in DAB converters," *IEEE Trans. Power Electron.*, vol. 36, no. 7, pp. 7395–7399, Jul. 2021.

Chuan Sun (Student Member, IEEE) received the B.Eng. degree in electronic and information engineering from the North University of China, Taiyuan, China, in 2015, and the M.Sc. degree in information technology from the Macau University of Science and Technology, Macau, China, in 2017. He is currently working toward the Ph.D. degree in power electronics with The Hong Kong Polytechnic University, Hong Kong, China.

From 2017 to 2018, he was an Electronic Engineer with Hangzhou Livoltek Power Company, Ltd., Hangzhou, China. His research interests include developing advanced modulation and control strategies for bidirectional resonant and nonresonant dual-active-bridge dc-dc converters.

Junwei Liu (Member, IEEE) received the B.Eng. degree in water conservancy and hydropower engineering from the Huazhong University of Science and Technology, Wuhan, China, in 2012, and the Ph.D. degree in power electronics from the Department of Electrical Engineering, The Hong Kong Polytechnic University, Hong Kong, in 2018.

He is currently a Research Assistant Professor with the Department of Electronic and Information Engineering, The Hong Kong Polytechnic University, Hong Kong, China. His research interests include power electronics, wireless power transfer, transportation electrification, and renewable energy systems.

Dr. Liu was the recipient of the Distinguished Reviewer Award from IEEE TRANSACTIONS ON INDUSTRIAL ELECTRONICS for the year 2022.

Xingyue Jiang is currently working toward the Ph.D. degree in electronic and information engineering with The Hong Kong Polytechnic University, Hong Kong.

His research interests include peer-to-peer energy trading, energy path planning, and energy Internet.

Lingling Cao (Member, IEEE) received the B.S. and M.S. degrees in electrical engineering from the Nanjing University of Aeronautics and Astronautics, Nanjing, China, in 2008 and 2011, respectively, and the Ph.D. degree in power electronics from The Hong Kong Polytechnic University, Hong Kong, China, in 2015.

She is currently an Associate Professor with the Harbin Institute of Technology, Shenzhen, China. Her research interests include power converter topologies and control strategies for renewable energy systems.

Yun-Chong Wang (Member, IEEE) was born in Liaoning, China, in 1987. He received the B.S. and M.S. degrees from Zhejiang University, Hangzhou, China, in 2010 and 2013, respectively, and the Ph.D. degree from the Hong Kong Polytechnic University, Hong Kong, in 2017, all in electrical engineering.

Since 2020, he has been an Associate Professor of Electrical Engineering with Zhejiang University. He has authored more than 30 technical papers. His research interests include the design and control of permanent magnet machines, novel electrical motors for electrical vehicles, hybrid electrical vehicles and renewable energy conversion system.

Jian-Xin Shen (Senior Member, IEEE) was born in Huzhou, China, in 1969. He received the B.Eng. and M.Sc. degrees from Xi'an Jiaotong University, Xi'an, China, in 1991 and 1994, respectively, and the Ph.D. degree from Zhejiang University, Hangzhou, China, in 1997, all in electrical engineering.

He was with Nanyang Technological University, Singapore. from 1997 to 1999, the University of Sheffield, Sheffield, U.K., from 1999 to 2002, and IMRA Europe SAS, U.K. Research Centre, Brighton, U.K., from 2002 to 2004. Since 2004, he has been a Professor of Electrical Engineering with Zhejiang University, Hangzhou, China. He has authored more than 320 technical papers, and holds more than 40 patents. His research interests include topologies, control and applications of permanent magnet machines and drives, and renewable energies.

Dr. Shen is an IET Fellow. He was the recipient of the Prize Paper Award from the IEEE Industry Applications Society and best paper awards from eight international conferences, and the 2019 Nagamori Award with recognition of his contribution to high speed electrical machines. He is a Member-at-Large of the IEEE Industry Applications Society, a member of the IEEE Nikola Tesla Award Committee, and a Distinguished Lecturer of the IEEE Vehicular Technology Society. He was the General Chair of three IEEE sponsored international conferences. More information of Dr. Shen can be seen at https://person.zju.edu.cn/en/jxs.

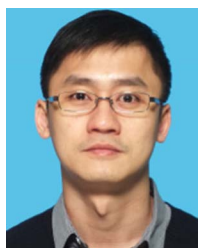

Ka-Hong Loo (Member, IEEE) received the B.Eng. (hons.) and Ph.D. degrees in electronic engineering from the University of Sheffield, Sheffield, U.K., in 1999 and 2002, respectively.

From 2002 to 2004, he was the Japan Society for the Promotion of Science Postdoctoral Fellow with Ehime University, Matsuyama, Japan. Since 2006, he has been with The Hong Kong Polytechnic University, Hong Kong, China, where he is currently an Associate Professor with the Department of Electronic and Information Engineering. His research interests include power electronics for renewable energy systems.

Dr. Loo has been an Associate Editor for the IEEE TRANSACTIONS ON ENERGY CONVERSION, since 2013, and *IEEE Open Journal of Circuits and Systems*, since 2019, and a Reviewer for various international journals and conferences. He is currently the Chair of the Power Electronics and Control Sub-Committee of the IEEE Technical Committee on Transportation Electrification.

Authorized licensed use limited to: Macau Univ of Science and Technology. Downloaded on May 08,2025 at 08:12:51 UTC from IEEE Xplore. Restrictions apply.